UNIVERSIDAD NACIONAL AUTÓNOMA DE MÉXICO

PROGRAMA DE MAESTRÍA Y DOCTORADO EN INGENIERÍA
MECÁNICA – MECATRÓNICA

DEVELOPMENT OF A SYSTEM TO MEASURE FORCE AND DEFLECTION OF THIN POLYMER MEMBRANES BONDED TO PLASMONIC METALLIC SURFACES.

TESIS
QUE PARA OPTAR POR EL GRADO DE:
MAESTRO EN INGENIERÍA

PRESENTA:
ING. ALDO EMMANUEL GONZÁLEZ LÓPEZ

TUTOR (ES) PRINCIPAL(ES)
DR. GABRIEL ASCANIO GASCA, ICAT-UNAM
DR. CARLOS ROBERTO ESCOBEDO CANSECO, QUEEN'S UNIVERSITY

CIUDAD DE MÉXICO, DICIEMBRE 2022

JURADO ASIGNADO:

Presidente: Dr. Alberto Caballero Ruíz.

Secretario: Dr. Carlos Roberto Escobedo Canseco.

1er Vocal: Dr. Gabriel Ascanio Gasca.

2do Vocal: M. I. Serafín Castañeda Cedeño.

3er Vocal: M. en I. Benjamín Valera Orozco.

Lugares donde se realizó la tesis:

Instituto de Ciencias Aplicadas e Ingeniería, Universidad Nacional Autónoma de México.

Chemical Engineering Department, Queen's University (Canada).

TUTORES:

_____

FIRMA

ACKNOWLEDGEMENTS

I am extremely grateful to my supervisors Professor Gabriel Ascanio and Professor Carlos Escobedo for their guidance and unconditional support through this process. I also want to express my deepest gratitude for the mentorship and intellectual input from Dr. Juan Manuel Gomez Cruz during the conceptualization and development of the sensing device, as well as during the experiments. Words cannot express my gratitude to Dr. Juan Manuel Gomez Cruz for our friendship, which I appreciate because it made my stay in Canada a comfortable and unforgivable experience, where I learned so many things about engineering and friendship and personal development. Thank you, Juan.

This endeavor would not have been possible without the support of my mother Leticia Lopez and my father Antonio Gonzalez, who taught me the basis to be the person I have become and gave me all the tools to pursue all my dreams. Many thanks to my brothers Antonio, Daniel, and Edgar for all their support. I love you all.

I want to thank my friends that I made in Canada, Carolina, Arthur, Brianna, Fatima, Swapnil, Annalise, Yazan, and Lily, because they made my stay a beautiful experience and taught me so many things during this time, that I don't know how to thank them. Special thanks to Karen for all your support and trust through all these years, and for making me a better person every day, thank you very much.

A special thank you to my professors Alvaro Nunez, Salvador Sanchez, and Juan Ocariz because they gave their sincere support and their wise advice since I was an 18-year-old student at UNAM.

The development of the sensing device and experiments were conducted in the Escobedo Lab at Queen's University. I would like to acknowledge ELAP, ICAT, and CONACyT for making my research stay at Queen's University possible. Finally, I will always be grateful to my alma mater, UNAM, and all the professors and friends that made me the engineer and the person that I have become.

SUMMARY

Polydimethylsiloxane (PDMS) is a widely used polymer in many research areas such as microfluidics, flexible electronics, soft robots, biosensors, biomedicine, among others. PDMS has various advantages compared to other materials; however, it presents weak bonding strength to many substrates. This work presents a new measuring system to measure bonding strength between a PDMS thin membranes and gold plasmonic surfaces.

This work is based on a piezoresistive sensor, it was selected as the main sensor to measure the force and a micrometer was adapted to a stepper motor to measure the displacement of the surfaces. Additionally, a digital camera was added to the system to bring more information about the adhesion phenomena. A calibration was performed to calculate the main characteristics of the instrument, sensitivity, range, precision, etc. This calibration shows the relationship between voltage and weight. Two different gold surface modification processes were studied to compare the presented device response to the current measuring systems and establish the presented solution as a cost-effective alternative.

RESUMEN

Polidimetilsiloxano (PDMS) es un polímero utilizado en muchas áreas de investigación como microfluidos, biosensores, biomedicina, electrónica flexible, robots suaves, entre otras. PDMS tiene muchas ventajas respecto a muchos materiales; sin embargo, presenta fuerzas de unión débiles con diferentes substratos. Este trabajo presenta un nuevo sistema de medición para medir la fuerza de unión entre membranas de PDMS y superficies plasmónicas de oro.

Este trabajo está basado en un sensor piezoresistivo, el cual fue seleccionado como el principal sensor de fuerza; y un micrómetro que fue adaptado a un motor a pasos para poder medir el desplazamiento de las superficies de prueba. Además, fue utilizada una cámara digital para obtener más información sobre el fenómeno de adhesión. Una calibración fue realizada para calcular las características principales del sensor, sensibilidad, rango de operación, precisión, etc. La calibración muestra la relación entre voltaje y peso, con la cual se probaron varias pruebas de oro con PDMS. Dos distintas funcionalizaciones fueron probadas en la superficie de oro, esto para comparar los resultados con sistemas existentes y establecer el sistema como una opción económica respecto a dichos sistemas.

CONTENTS

FIGURES

1 INTRODUCTION

1.1 Surface Plasmon Resonance Based Sensors

Optical sensors are widely used to measure chemical and biological quantities. Many sensors with different operational principles can be employed for that task. The most popular methods are ellipsometry, spectroscopy, interferometry, spectroscopy of guided modes in optical waveguides, and surface plasmon resonance. Among these methods, the Surface Plasmon Resonance (SPR) based sensors, have been studied due to their high sensitivity [1].

In 1902 Wood documented for the first time the plasmon effect when he illuminated a metallic diffraction grating with polychromatic light. On his observations he noticed dark narrow lines, which he could not explain, and he named them “anomalies”. In that work, he discussed the possible explanation, attributing these anomalies to the light diffraction when it hits the ridge of the grating [2].

A plasmon is a collective oscillation of free electrons in a noble metal; in other words, a plasmon is a quantum of a plasma oscillation. Another interpretation of plasmon is that represents a mechanical oscillation of the electron gas of a metal. According to Mayer and Hafner, 2011 Surface Plasmons are optically excited, and light can be coupled into standing or propagating surface plasmon modes through a grating or a defect in the metal surface [3].

Surface Plasmon Resonance (SPR) is an oscillation that takes place on the bond of surfaces with two dielectric constants of opposite signs, such as metal and dielectric materials. These materials have been widely used in the development of SPR sensors [1]. The SPR sensors have shown a high sensitivity to changes in the reflection index near the metallic surface [4].

Possible configurations of SPR sensors are shown in Figure 1, namely: Attenuated Total Reflection (ATR), or Kretschmann configuration; optical grating configuration, and nanohole array configuration. In addition, another widely investigated configuration is the Localized Surface Plasmon Resonance (LSPR) sensor, where nanoparticles are excited by light with larger wavelengths than the particle diameter [4].

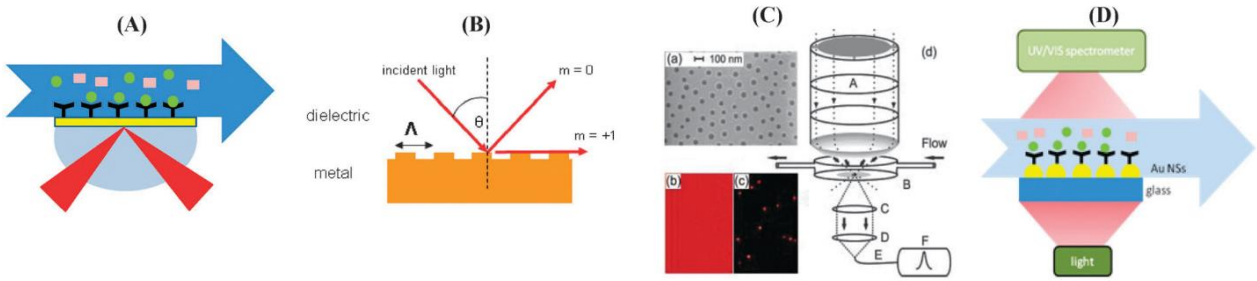

Figure 1: A) Attenuated Total Reflection or Kretschmann configuration; B) Optical gratings configuration; C) SPR sensor based on nanohole arrays; and D) Localized Surface Plasmon Resonance sensor [4].

Nanoplasmonic sensors show extraordinary sensitivity compared to current optical sensors, moreover, this kind sensor has shown ability of real time, label-free sensing. They have shown successful applications in the field of chemistry, biology, medicine, and food safety [5].

The structure of an SPR-based sensor has three main parts. The first one is an optical system, which excites the system and produces surface plasmons. The second one is a transducer, which interrelates the optical and (bio)chemical domain. The last part is the electronic system, which supports optoelectronic components of the sensor and allows data processing [1].

Among the possible configurations for SPR-based sensors, the integration of nanohole arrays has been widely studied, because they facilitate the resonance-induce field enhancement [6]. In addition, the development and application of SPR-based sensors has increased in the past few years and a focus has been the reduction in cost to incorporate them into devices for biological and chemical sensing applications [7,8].

In recent years, the integration of nano hole array-based sensors to microfluidic chips allowed the development of optofluidic devices with unique characteristics compared to other optical sensors [6]. Nano hole arrays made from gold have shown impressive

performance as optical detectors in various investigations, therefore, this material is widely used on these applications [6]. In general, microfluidic chips are made of glass or PDMS, being PDMS the most popular nowadays [9]. In consequence, the bonding properties, in particular bonding strength, of the main materials for nano hole arrays (gold) and microfluidic chips (PDMS), is a promising area to study the implications of this property on the performance of new optofluidic devices.

1.2 Bonding strength of PDMS to gold surfaces

In general, microfluidic devices are made of various materials such as elastomers, glass, and metals [10]; however, in recent years, research on elastomers bonded to metals on microfluidic devices have increased due to their properties. In many applications these materials interrelate, making their surface interaction an important feature to study. Different materials, such as gold, silver, glass, and silicon, present useful surface properties[10]. From those materials, according to Prats-Alfonso et al (2011), gold is one of the most versatile materials, being this material commonly used to create biosensors destinated for different applications, such as medical diagnostic and industrial processes. Polydimethylsiloxane (PDMS) is a polymer that belongs to the siloxanes group. It is usually presented in two separate parts, a liquid silicon rubber base, and a catalyst or curing agent. PDMS is widely used in electronics, mechanics, biology, chemistry, and microfluidics, among other research areas, due to its properties; it is transparent to optical wavelengths, inexpensive, flexible, thermal, and chemically stable, and also is biocompatible [11,12]. Also, PDMS is a suitable material for thin membranes, because of its semi permeable behavior, which allows gasses passing through but not water, this characteristic can be used on biosensors and Lab-on-Chip applications [13,14]. However, some properties of PDMS could represent drawbacks for biosensing, such as its hydrophobicity or the need to improve the wettability to deliver liquids [9]. This problem arose the need for some treatments (preprocess or post-process) for this polymer [15].

Due to the advantages of using gold and PDMS at microscales, such as microfluidics, many studies have focused on the combination of PDMS membranes and gold surfaces [16]. Although some treatments allow bonding of PDMS to gold surfaces [17,15], some studies focus on the maximum pressures that bonding permits, before leakage occurs

due to bonding failure[17]. Casanova-Moreno et al (2017), use microchannels to test bonding between PDMS and gold pattern surfaces, they concluded that some treatments are capable of improving the mechanical properties of the bonding between these two materials.

Some studies have focused on test bond strength of PDMS to gold films by using peeling tests with adhesive tape [18,19], for example, Byun *et al* (2013), uses this method to compare the performance of gold surfaces modified with MPTMS and 11MUA. This method showed that gold and PDMS bond is stronger by using MPTMS treatments; however, this method is qualitative but not accurate. On a different study, Ouellet et al, (2010), used a strength testing machine (MTS 810) to obtain the force needed to separate PDMS from modified gold surfaces; although this process is more accurate, the cost of this machine (MTS 810) can make it unaffordable for further studies [20].

1.3 Force and stress sensors

Transducers are devices that convert one form of energy into another. According to the International Vocabulary of Basic and General Terms in Metrology (ISO, 2006), a sensor is defined as a "*component of a measuring system that is directly affected by a phenomenon, body, or substance carrying a quantity being measured"* [21]*.* It is important to notice that this definition is general, and many authors use a narrower definition by including that a sensor must have an electrical output signal [22]. An actuator is considered as the opposite of a sensor, due that the actuator oversees the conversion of electrical signals into actions, such as mechanical.

A sensor can be integrated by many transducers and one direct sensor, these elements oversee the correct conversion of the stimulus into the desired electrical signal, this sensor is called hybrid [23].

Sensors can be classified according to the application, the sensing elements, the input stimulus or the operational principle [24,25]. Measuring forces and stress is an important field of study, a broad range of applications needs to measure forces accurately, for instance, in robotics, wearable sensors where the development of force sensors to measure the behavior of robots is crucial to perform different tasks [26] such as wearable sensors to healthcare, monitoring, and medical treatment. There are distinct sensors

for measuring forces; based on their operational principle, they can be separated into many groups, for instance, capacitive, resistive, and piezoelectric sensors. [27]

Stress could be due to tension or compression forces; stress is defined as a force per unit area. The strain is the result of stress, and it is a dimensionless quantity, meanwhile, the stress is a quantity that has physical dimensions. Many of the sensors can measure the stress by knowing the strain of a material and the Young's modulus. [22]

The interest on bonding strength properties between gold and PDMS has caused the use of measuring systems separated on four main tests, namely: Tensile strength test (Figure 2 a); shear strength test (Figure 2 b); peeling test, (Figure 2 c); and leakage test [13]. From these tests, the tensile strength and the shear strength tests are performed by applying normal or tangent forces to the polymeric surface and measuring the applied force required to separate the gold and the PDMS[13].

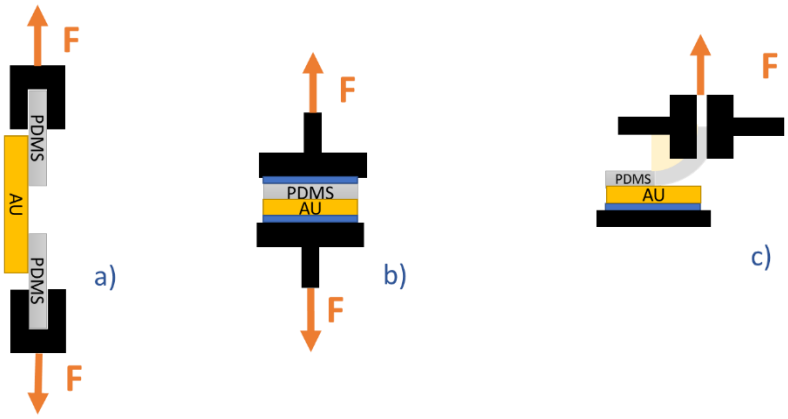

Figure 2 Most common bonding strength testing methods: a) shear strength test; b) tensile strength test; and c) peeling test. Schematic adapted from [12].

1.3.1 Capacitive sensors

Capacitive sensors are based on the two-conductor surfaces called electrodes, which are separated with a dielectric material. The electric charge (Q) between the electrodes is directly proportional to the voltage (V) between them and the capacitance (C).[28]

$$Q = VC \qquad 1$$

The capacitance is a quantity that depends on three parameters: the permittivity (ε) of the dielectric material, the surface area (A), and the distance between the electrodes (d), as expressed in the equation 2:

$$C = \varepsilon \frac{A}{d} \qquad 2$$

These sensors are widely used to measure displacement, force, and pressure. They are well known because of their low cost, and high sensitivity, and they are also available in commercial A/D chips, making them accessible nowadays. The main drawbacks of these sensors are the high hysteresis effect; their sensitivity to weather conditions (moisture); and the complex electronic circuits required to use them. [29] [28]

There are three basic configurations for these sensors: flat plate, multiplate, and silicon capacitive sensors. The flat plate and the multiplate configurations are commonly used to measure displacement; meanwhile the silicon capacitive sensors are also used to measure distance, force, and pressure.[28] Additionally to these configurations, a cylindrical configuration is also available, but in practice it is difficult to build it compared to the flat plate and multiplate configurations. [23]

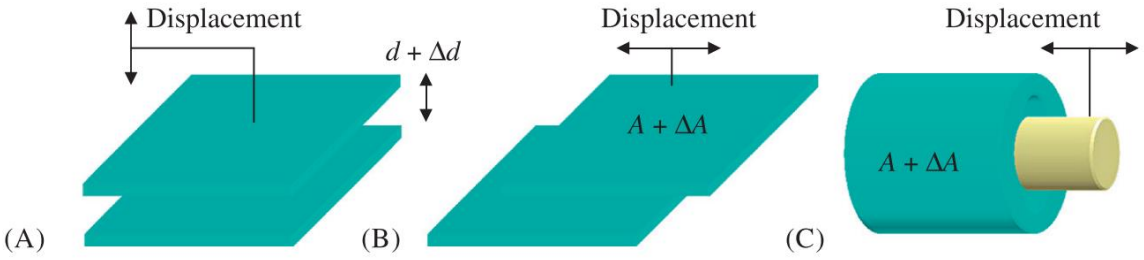

Figure 3 Configuration of capacitive sensors used to measure displacement [28].

Figure 3 shows the three basic configurations for measuring displacement using capacitive sensors, flat plate configuration (A and B), and cylindrical configuration (C). It is important to notice that by using an appropriate construction, any displacement sensor could be used as a force sensor [28].

In contrast to flat plate configurations, the silicon pressure sensor, shown in Figure 4, incorporates a flexible membrane attached to one flat electrode allowing the variation of the voltage due to changes in the distance between the electrodes (reference gap).

Two main structures of this kind of sensor are (A) a glass top plate configuration and (B) three silicon layers [28].

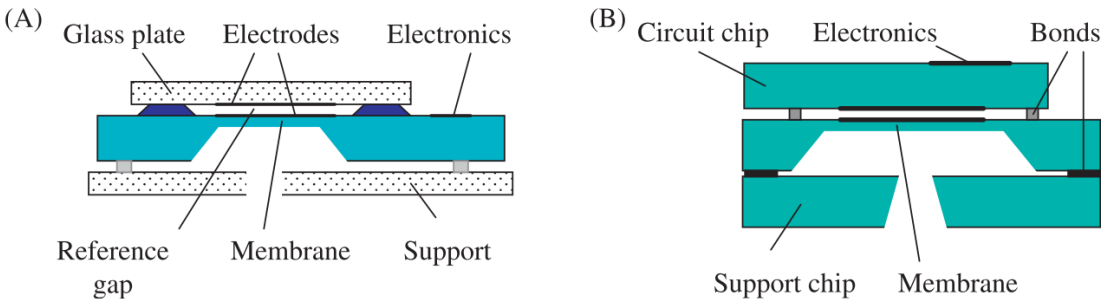

Figure 4 Basic structures of integrated capacitive pressure sensors [28].

1.3.2 Piezoelectric sensors

The piezoelectric effect is present on specific materials when they are deformed, producing the reorientation of electric charges in the material, also called electric polarization. By changing the electric polarization, the elements have opposite charges on the opposing surfaces of the element. In these materials, the change in charge is proportional to the applied force.[30] Piezoelectricity comes from the Greek "piezein" which means «*to press, to compress*» and refers to the electricity, then it is known as electricity from pressure or compression. In 1880, the Curie brothers discovered this effect; years later, they documented the inverse effect on this kind of material [31].

Three groups of materials exhibit piezoelectricity: the natural piezoelectric materials, the quartz (SiO_2); ceramic materials, such as barium titanate (BTO); polymers, for instance, polyvinylidene fluoride (PVDF) [30].

The construction of these sensors is similar to a flat-plate capacitor, where the dielectric element is located between two electrodes, and the strain due to external forces charges the capacitor. Some piezoelectric sensors use two electrodes on opposite sides to measure a voltage between the two electrodes [23,30]. In Figure 5 the piezoelectric effect is represented on quartz when compression is applied (b) or tension (c) on two edges of the crystal [23].

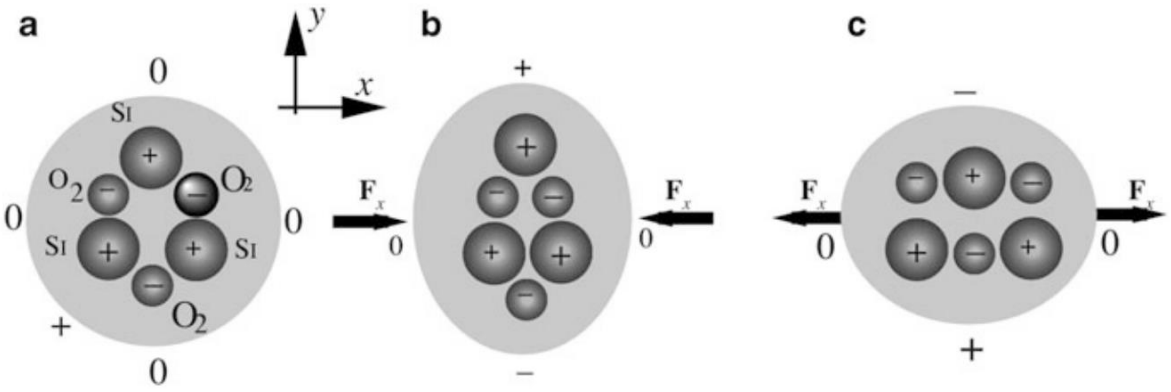

Figure 5 Piezoelectric effect in quartz crystal [23].

The magnitude of the piezoelectric effect can be represented by the vector of polarization [23]:

$$\boldsymbol{P} = \boldsymbol{P}_{xx} + \boldsymbol{P}_{yy} + \boldsymbol{P}_{zz}$$

These vectors can be written as the linear combination of the axial stresses:

$$\boldsymbol{P}_{xx} = d_{11}\boldsymbol{\sigma}_{xx} + d_{12}\boldsymbol{\sigma}_{yy} + d_{13}\boldsymbol{\sigma}_{zz}$$

$$\boldsymbol{P}_{yy} = d_{21}\boldsymbol{\sigma}_{xx} + d_{22}\boldsymbol{\sigma}_{yy} + d_{23}\boldsymbol{\sigma}_{zz}$$

$$\boldsymbol{P}_{zz} = d_{31}\boldsymbol{\sigma}_{xx} + d_{32}\boldsymbol{\sigma}_{yy} + d_{33}\boldsymbol{\sigma}_{zz}$$

Where $\boldsymbol{\sigma}_{xx}, \boldsymbol{\sigma}_{yy}$, and $\boldsymbol{\sigma}_{zz}$ represents the axial stresses, and d_{ij} are the piezoelectric coefficients, which are unique for each material and depends on the force direction; the units for these coefficients are $\left(\frac{C}{N}\right)$, Coulomb per Newton. If a piezoelectric material is properly built as a flat plate capacitor configuration, and the applied force lays on one axis only, then the charge generated by the piezoelectric Q_x will be [23]:

$$Q_x = d_{11}F_x \qquad 3$$

Where F_x is the applied force, and d_{11} is the piezoelectric coefficient along the *x* axis. Considering this piezoelectric sensor as a capacitor due to the electrodes on its edges, the voltage generated (V) is expressed as:

$$V = \frac{Q_x}{C} = \frac{d_{11}}{C}F_x \qquad 4$$

The capacitance of this configuration is defined as:

$$C = \frac{\kappa\varepsilon_0 a}{l} \quad (5)$$

Where a is the electrode surface area, l is the crystal thickness and $\kappa\varepsilon_0$ is the dielectric constant. With this equation, the output voltage of the sensor can be expressed as:

$$V = \frac{d_{11} l}{\kappa\varepsilon_0 a} F_x \quad (6)$$

As this equation shows, the maximum output voltage can be obtained as the electrode surface area is minimized, and the thickness is increased. Although this expression shows the linear relationship between force and voltage, this kind of sensor is not suitable to measure static forces. [23]

Piezoelectric sensors are widely used in industry and research to measure force and by using a proper construction; they also can measure pressure, strain, and acceleration. For detecting forces, piezoelectric sensors are sensitive to small deformations and do not need the implementation of spring systems.[30]

1.3.3 Resistive sensors.

Resistive sensors are devices that measure changes in the environment based on changes in the resistance of a transductor. All the materials have different electrical properties associated with them, for instance, resistivity and conductivity. Conductivity σ is defined as the relation between the current density J and the electric field E applied to an element, also it can be seen as the inverse of the specific resistivity ρ.[23,32]

$$\sigma = \frac{1}{\rho} = \frac{J}{E} \quad (7)$$

The specific resistivity ρ is expressed in the next equation:

$$\rho = \frac{m}{ne^2\tau} \quad (8)$$

Where τ, is the time between collisions, e is charge of an electron, m is the mass of electron and n is the number of conduction electrons per unit volume of material.[23] Some factors also affect the specific resistivity of a material, like temperature, strain, and moisture.

The resistance of a bar B depends on the geometry and the properties of the material. The resistance between the endpoints of the bar B of length l and cross-section area A is represented by:

$$R = \rho \frac{l}{A} \qquad 9$$

The resistance R of a resistor in electrical circuits can be determined, first by applying a voltage V on the element, which generates an electrical current I, and then using Ohm's law:[23]

$$V = RI \qquad 10$$

Based on this equation, resistive sensors can be divided into five main groups; strain gauges, which are based on the variation of the ratio $\frac{l}{A}$ and are widely used as force and pressure sensors; piezoresistive sensors, which are used to measure force and pressure; magnetoresistive sensors, used to measure changes on magnetic fields; thermoresistive sensors, which are more sensitive to temperature variations and opto-resistive sensors, which are sensitive to light variation. The last four groups of sensors are based on the variation of the specific resistivity ρ. [32]

1.4 Piezoresistive sensors

1.4.1 History

The discovery of the piezoresistive effect can be attributed to Lord Kelvin in 1856, who compared the change of the resistance in copper and iron wires, while their elongation was the same. In 1935 Cookson defined "piezoresistance" as the change in conductivity with stress. Piezo comes from the Greek "piezein" which means <<*to press, to compress*>> and from Latin "resistĕre", which means <<*to stop*>>. Piezoresistive is the change in the resistance due to a change in pressure or compression. [33,34]

1.4.2 Piezoresistive effect

The resistive sensors are based on wires, on which relative changes of the resistance are stated in the equation:

$$\frac{dR}{R} = \frac{d\rho}{\rho} + \frac{dl}{l} - \frac{dA}{A} \qquad 11$$

The wire has across sectional

area defined as $A = \pi r^2$ and derived from this equation results on:

$$\frac{dA}{A} = 2\frac{dr}{r} \qquad 12$$

The relation between the resistance variation and its parameters could be expressed as:

$$\frac{dR}{R} = \frac{d\rho}{\rho} + \frac{dl}{l} - \frac{2dr}{r} \qquad 13$$

To simplify this expression, it is necessary to use the Poisson's ratio, which states for the relationship between the change on the radio and the length of the wire.

$$\nu = -\frac{dr/r}{dl/l} \qquad 14$$

Finally, by substituting equation 14 in equation 13 the relative change in resistivity is expressed as:

$$\frac{dR}{R} = \frac{d\rho}{\rho} + (1 + 2\nu)\frac{dl}{l} \qquad 15$$

The gauge factor for a resistive sensor is defined as the fractional change in resistance per unit strain:

$$GF = \frac{\frac{dR}{R}}{\frac{dl}{l}} \qquad 16$$

This factor is important because it represents the sensitivity of piezoresistive sensors [25].

Equation 15 implies three possible cases for resistive sensors: the first case when the change ratio on the resistivity is bigger than the geometrical factor:

$$\frac{d\rho}{\rho} \gg \frac{dl}{l} \qquad 17$$

In this case, the geometrical changes are negligible and then changes on volume resistance are expressed as:

$$\frac{dR}{R} = \frac{d\rho}{\rho} \tag{18}$$

In this scenario, the change in resistance will depend only on material's specific resistivity, so that equation 18 allows having larger gauge factors than other cases of study.

The second case is when changes on the geometrical factor and the specific resistivity are comparable to each other:

$$\frac{d\rho}{\rho} \sim \frac{dl}{l} \tag{19}$$

Considering equation 19 the change in the volume resistance is represented as:

$$\frac{dR}{R} = (2 + 2\nu)\frac{dl}{l} \tag{20}$$

And the gauge factor should be determined only by the Poisson's ratio (ν) and this is constrained by $\nu \leq 0.5$. In consequence the maximum gauge factor for this case is 3, which is a small factor for a sensor.

The third case is characterized by bigger changes in the geometrical factor:

$$\frac{dl}{l} \gg \frac{d\rho}{\rho} \tag{21}$$

On this regard, the volume resistance is represented by the expression:

$$\frac{dR}{R} = (1 + 2\nu)\frac{dl}{l} \tag{22}$$

In this case, changes in the resistance are due to the geometrical changes, therefore the gauge factor will be maximum 2.

In conclusion, change in the specific resistivity ($d\rho/\rho$) and the geometrical factor (dl/l) exists for all the resistive sensors, which means that all piezoresistive sensors are sensitive to these changes. For instance, strain gauges (metal materials) are more

sensitive to geometrical factors (dl/l) and are mainly used in the case number three, sometimes the specific resistivity factor is almost zero; meanwhile, on piezoresistive sensors (semiconductor materials) the variation in the resistivity is 50 or 100 times larger than the changes in the geometrical factor, which represents the first case [23,32,34,35].

1.4.3 Types of piezoresistive sensors.

According to the operational principle of the sensors, piezoresistive sensors are divided into two main groups, namely: strain gauges and Force-Sensing Resistance (FSR) sensors. Strain gauge sensors are the most used due to their large number of applications.

1.4.3.1 Strain Gauges

Piezoresistive sensors can transform stress and strain into resistance variation, but strain is easier to measure, then when a sensor directly measures the strain is called Strain Gauge, which is a passive sensor and can be separated in terms of its configuration [36].

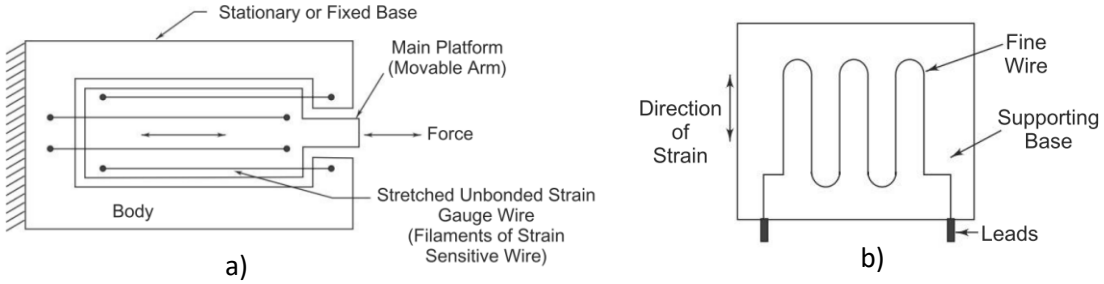

Figure 6: a) Unbonded strain gauge b) Bonded strain gauge.

Among strain gauges, there are three main divisions, namely: wire strain gauges, foil strain gauges and semiconductor strain gauges. Wire strain gauges can be classified into bonded (Figure 6 a) and unbonded (Figure 6 b) strain gauges. The latter has wires bonded to a supporting base, and then the strain is transferred to the wires. Meanwhile, the unbonded strain gauges are wires joined between two parts of insulating material and then the length is varied with a mobile platform. These gauges are in the second group and its gauge factor is between 2 and 3 [36].

A problem with bonded strain gauges is that in presence of strain wires will experiment strain in the transverse axis. This effect is not desirable because introduces error signals; despite this resistance change in the cannot be eliminated, but it can be compensated by using different configurations that can consider this phenomenon[36].

Foil strain gauges were implemented by using a metallic foil to make the patterns on these devices. Building process of these sensors consists of attaching a thin foil to a base and then applying a mask to the desired pattern Finally, the remain metal is eliminated. Using this process, the metal patterns can be thinner than the wire strain gauges, and the sensitivity of these groups is almost the same. Recently, most of the metallic strain gauges are built on this configuration because it reduces the hysteresis and the transverse sensitivity, and increases the longitudinal sensitivity compared to the wire configuration [36,37].

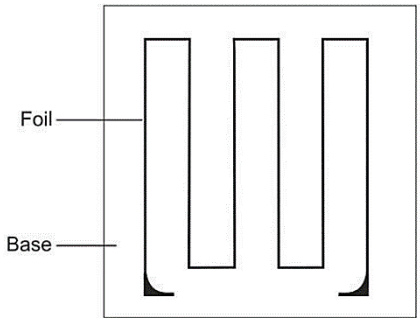

Figure 7 Foil strain gauge.

The use of semiconductor materials as piezoresistive sensors have been widely investigated due to properties of these materials; germanium and silicon are examples of them. The advantage of using these materials instead of metals are, as seen in the first case of the piezoresistive sensors, the gauge factor of these sensors is between 50 and 400 and the range of hysteresis approximately 0.05% On the other hand, they are more expensive than wire strain gauges and their behavior is less linear [37]. One of the recommended circuits for this sensor are invert-current operational amplifiers to act as a pressure transductor, and a Wheatstone bridge array to compensate the temperature variations [36].

1.4.3.2 Force Sensing Resistors (FSR)

Force Sensing Resistors are sensors based on two main elements, first, a thin resistive layer applied to a film and digitizing contacts applied to another film. When forces are applied to these devices, the contact between the two films varies depending on this force, in consequence, the resistance of the former film will decrease [25]. FSR can be classified into two groups depending on the configuration, namely: Thru mode (five layers) or Shunt mode (three layers).

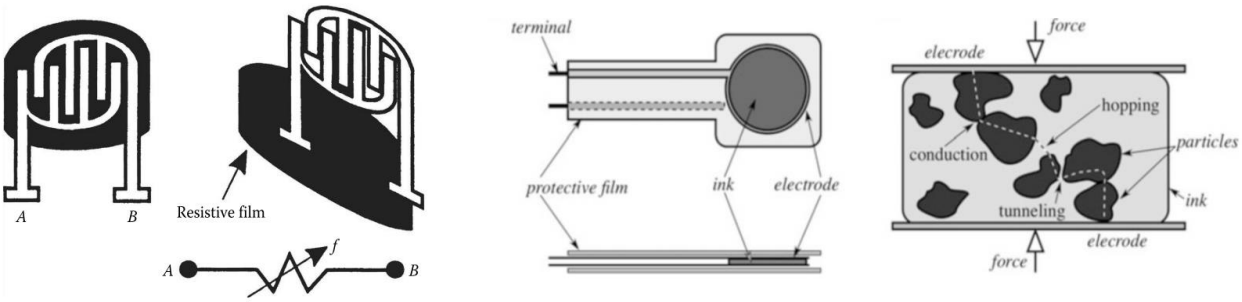

Figure 8: a) FSR sensor; b) Composition of a FSR sensor; and c) Operating process of ink based FSR sensor.

Thru mode consists of five layers, two protective layers, the printed film and finally two electrodes. The Shunt mode for FSR sensors comprises three layers, one of which has some conductive materials impregnated on it, for example, carbon powder [23].

A FSR sensor exhibits higher thermal stability compared to semiconductor strain gauges, and the sensitivity is at least ten times larger than wire strain gauges [23]. Moreover, these sensors have a logarithmic behavior based on resistance changes [25], as shown in Figure 9 , but present a quasilinear behavior when the conductance is measured [23].

FSR sensors show lower sensitivity to temperature changes compared to the semiconductor strain gauges. To have a linear behavior, the sensor must have an offset to start measurements (usually 40g). Studies have shown the comparison between FSR sensors, piezoelectric sensors, and capacitive sensors [38,39]. Such researches have demonstrated that FSR sensor are cost-effective sensors that can be used for many applications.

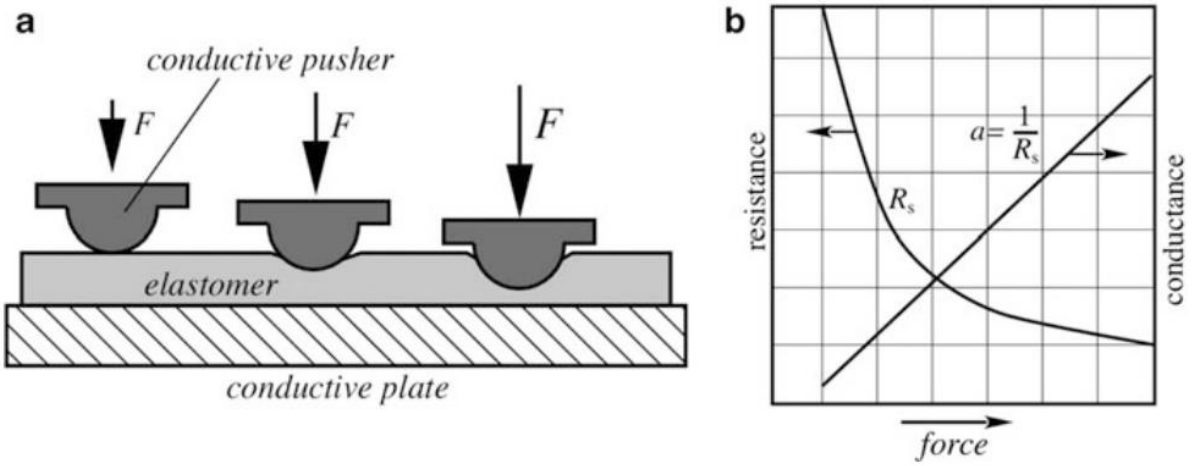

Figure 9 a) FSR tactile sensor elastomer film; b) General transfer function of FSR sensor, resistance, and conductance.

1.4.4 Applications of FSR sensors

FSR sensors have been widely used for accurate applications, such as measuring heartbeats [23], sensors for robotic fingers [39], foot plantar pressure measurement [40], musculoskeletal behavior and sport tracking [38], instrumental gloves [41], etc.

On this regard, it is shown that FSR sensors can be used on various applications in different fields. Many researchers use different circuit configurations to obtain different sensor characteristics, such as sensitivity, sensor span and accuracy [39,42,43]. Among the limitations of the FSR sensors, it is shown by many authors that the hysteresis effect, the drift effect, and the use of cycling forces are substantial sources of error and inaccuracy for the systems that work with this kind of sensor [44]. Another important limitation is the room temperature, which should be controlled or at least the room temperature must be the same as possible as the calibration curve conditions [42].

1.5 Sensor static characteristics.

Static characteristics of a sensor are the properties of this device obtained from a process called calibration, these are: sensitivity, sensor span (input full-scale), resolution, errors, accuracy, linearity, drift, full-scale output, resolution, repeatability, and hysteresis. These characteristics can be considered when two different sensors are compared, to choose the best option [23,36].

1.5.1 Sensitivity

Sensitivity is defined as the relationship between the output and the input of the system when a change in the input is applied. When a system is represented by a linear function, then the sensitivity is the slope of the calibration curve. Assuming that the linear representation of the system is defined by:

$$y = A + B * x \tag{23}$$

Where A is the offset of the sensor, B is the slope of the line, y is the output of the system and x is the input or stimulus. Thus, the sensitivity of the system will be expressed as:

$$B = \frac{\Delta y}{\Delta x} \tag{24}$$

For nonlinear curves, the sensitivity is not represented by a number, it is defined as the derivative of the nonlinear function between the output and the input, evaluated on the input point x_i [23].

1.5.2 Sensor span

Sensor span or input full-scale is defined as the range of stimuli that the sensor is capable of measuring. This value is the highest input value before having an output beyond the tolerance. Graphically the span is the zone in the stimulus axis where all the data is found [25].

1.5.3 Errors

The error is the deviation of the measured value from the desired value. The error can be expressed in two forms, in absolute and percentage [36]:

$$e = Desired\ value - Measured\ value = Y_n - X_n \tag{25}$$

$$\%Error = \frac{Absolute\ value}{Expected\ value} \times 100 = \left(\frac{Y_n - X_n}{Y_n}\right) \times 100 \quad (26)$$

Where Y_n is the desired value and X_n measured value.

Authors categorized errors to understand and treat the source of errors, to do this they are divided into three main groups according to the nature of the error:

1.5.3.1 Gross error:

These errors are mainly due to human intervention on recording observations, which results in mistakes, also incorrect adjustments or computational mistakes can be categorized as gross errors. It is important to note that gross errors cannot be solved by mathematical analysis [36].

1.5.3.2 Systematic error:

Systematic errors are due to defective or worn parts, mainly due to ageing or effects of the environment on the instrument. This group of error influences the measurements of a determined quantity [36].

1.5.3.3 Random error:

There are many effects that influence the sensor, it is an accumulation of many unknown small effects that take place only in one measurement. Sometimes the insufficient knowledge of the nature of the process and a poor design are the main causes of ignoring these errors in the system.

1.5.4 Accuracy

Accuracy is the specified amount of uncertainty of measured values [23], in other words accuracy is the highest deviation from the ideal value of the sensor. This concept is fundamental for a sensor, it represents the difference between a true value and the measured value, the true value is called like that because it can be referred to an absolute or agreed standard [25]. Authors express the accuracy of a system in terms of relative accuracy or percentage.

$$Accuracy = 1 - \left|\frac{Y_n - X_n}{Y_n}\right| \quad (27)$$

$$a = 100\% - \%error = A \times 100\% \quad (28)$$

1.5.5 Precision

Precision is a concept close to accuracy, the difference between them is that precision is the number of times that one measure will repeat, therefore, is also known as repeatability. This concept is important for a measuring system. To calculate the repeatability many, have to be done, then the average is calculated and the precision.

$$Precision = 1 - \left| \frac{X_n - \bar{X}_n}{\bar{X}_n} \right| \quad (29)$$

Where X_n is the nth measurement and $\bar{X}_n$ is the average of the nth measurement.

1.5.6 Linearity

Linearity is the maximum deviation of the real calibration curve from the theoretical value. Also, this characteristic is called nonlinearity, due that the behavior of the sensor is always nonlinear, but through approximations and data processes, a linear function describing the system can be obtained.

1.5.7 Drift

Drift is caused by variations on the sensor parts or environmental variables over time. Signal drifting is defined as a change in the signal output over time, without changes in the stimuli.

1.5.8 Full-scale output

It is the range in which the system can respond to the input signal, in other words, the minimum output and the saturation signal.

1.5.9 Resolution

Resolution is defined as the smallest change in the input variable that causes a change in the output.

1.5.10 Hysteresis

The change in the direction of application of the stimulus will result in a different behavior of the sensor. This change is called hysteresis and it is well known in mechanics and magnetic fields.

1.6 Literature review

In recent years, PDMS has become a critical material for many research areas, such as microfluidics, biomedicine, flexible electronics, etc. [45,46,47] For example, in microfluidics this material plays a crucial role in the construction of chips to perform specific tasks [48]; in biomedical applications, the utilization of PDMS increased due to its key features and the low environmental impact [47,49,50]. In addition, many applications reported on research articles include the PDMS bonding as an important decision factor in substrate election. Some investigations are focused on PDMS bonding to polymers, for instance, polymethylmethacrylate (PMMA), polyimide (PI), polyethylene terephthalate (PET), polystyrene (PS), and PDMS itself [50–53] ; other researchers work with metallic materials, such as, gold, titanium, aluminum, copper, chromium, among others [45,48,50,54–58]. On this regard, some customized measuring systems have been developed to test bonding strength on polymer membranes, microfluidic chips, and biosensors [55,59–61]; regardless of these developments, most of the studies on this topic employs expensive and sophisticated equipment to perform measurements [51,52,58,62].

According to Borók et al (2021) manual peeling, peeling, tensile strength, shear strength, leakage, and burst are the most used tests to measure bonding strength. Manual peeling is the easiest method; however, it needs proper tools, also many assumptions are made to describe the bonds[13]. For example, Byun et al (2013) reported the use of this process to measure the performance of PDMS bonding strength; this report consists of a quantitative characteristic of the bonding[18]. In contrast, the peeling test employs instruments to measure direct forces on bonding sections. For example, Hoang et al (2016) presented a peeling test where they pulled at a 90° angle a substrate from PDMS, they employed a tester machine Instron 5943, and the paper shows the difference between four different bonding techniques; however, the results shown that the force applied is not uniform, and some peaks are present on the signal response [63].

The tensile strength test is the most used method of adhesion measurement [64];it consists of a uniaxial or biaxial force applied to the PDMS to detach the substrate; the force can be measured by strain gauges attached to the samples [61]. This type of test enables researchers to determine important properties of the material, for example, Young's modulus, yield strength, ductility, etc.; Nonetheless, tensile studies are not limited to mechanical properties, also measure electrical, magnetic, or optical effects on the substrates [58–60,65]. This method offers smooth and accurate results, although most of them make use of specialized and expensive machines [51,52,54,58,60,62].

Another method to measure the bonding performance is the shear strength test, the interest of it relies on overcoming the internal parallel forces of the PDMS-based chips [66]. Wang et al (2017), reported five stages on a shear strength test, these stages are attributed to bond breaking; however, the non-uniformity of the oxygen treatments and the surface finish of the substrate, increase the noise on measurements.

Finally, the leakage test is also widely used to test the PDMS adhesion; It is important to note that almost all the articles cited in this work, are based on the combination of two or more testing methods. Therefore, tensile and shear methods are widely used alongside leakage tests, this is due to the additional information that this method can bring [45,51–53,66–68]. For example, Rezal et al (2011) used a tensile test to determine the stress-strain curve of the PDMS bonded to parylene; in addition, they include the leakage test with different fluids, and they reported a big difference in the behavior of the strength depending on the fluid used [51]; Also, the maximum pressure obtained with the leakage test is different compared to the shear or tensile test used.

Customized methods have been developed as an option for sophisticated testing machines; these are based on different operational principles, for example, Lacour et al (2006) use micrometers to measure the response of PDMS to the strain; Read and Dally (1993), measured the elongation of a characterized spring to calculate the applied force to the PDMS. These devices have limitations, such as a limited linear range of operation, and assumptions of the acting forces, which made them less accurate than the previous works presented.

An optical analysis is extensively used on bonding strength measurements because it offers details about the nature of forces, and it helps to establish hypotheses about the measuring system behavior; in consequence, most of the systems presented here use an optical device, for example, microscopic cameras[56], digital cameras[55], contact angle measurements [58], among others.

In a conclusion, the bonding strength of PDMS is a determinant topic to study, due to the broad area of application of this polymer; in recent years there have been many papers about the key factors to achieve good adherence between PDMS and many substrates. However, these studies rely on the use of expensive machines. According to Agostini et al (2019), some of the current PDMS treatments to improve bonding are not sufficient, and future investigations will use bonding tests to develop new bonding methods In addition, customized measuring systems are a good option compared to existing machines because they can be designed to satisfy all the requirements of the samples; nevertheless, these instruments should overcome difficulties of instrumentation requirements, such as a good operating range and accurate results.

1.6.1 Commercially available options.

Current commercial solutions for measuring bonding were investigated to develop an alternative for this application. For example, Mark-10 presents a Universal Testing Machine, M5-2 which has a resolution of 0.2 grams and a full-scale output of 1kg, the sensor costs 1300 USD (Appendix A); however, this price does not include the motorized test stand, which costs 3200 USD. Another option used by Bakouche et al, 2020, is the Mecmesin Multitest, which has a resolution of 0.1 kg, a maximum input of 0.5 kN, and an accuracy of 0.1% FS, which represents ±51 g, the total cost is around 7000 UDS (Appendix B).

1.7 Goals and expectations

1.8 Primary Goal

Develop a cost-effective and accurate system capable of measuring the deflection and the total force applied to thin polymer layers bonded to plasmonic metallic surfaces, which are used in Surface Plasmon Resonance (SPR)-based sensors.

1.9 Secondary Goals

To meet the primary goal, the following steps will be followed:

- Investigate force sensors and their operational principle.
- Choose an appropriate sensor based on the system requirements.
- Design a mechanical system that allows transporting forces from the top plunger to the sensor.
- Design and build a circuit that obtains accurate data from the sensor.
- Test the sensor's response to external forces applied to the top of the plunger.
- Calibrate the sensor in an operating range according to the range of forces found in the literature on SPR-based sensors.
- Characterize the sensor to obtain parameters, such as repeatability, sensitivity, and accuracy of operation.
- Identify the type of errors present on the system's behavior.
- Run tests using different polymer membranes bonded to metallic surfaces, to compare the performance of the bonding process on each set of membranes.

2

DEVELOPMENT OF THE FORCE AND DEFLECTION MEASURING SYSTEM

2.1 Methodology

This chapter aims to get insight about the deflection of thin polymer membranes bonded to plasmonic metallic surfaces when forces are applied to these membranes. A new measuring system has been developed to measure the forces applied to polymer membranes and the total deflection they cause. This system transports forces to an appropriate force sensor and uses a micrometer to measure the total deflection on the membranes. In addition, a video camera has been employed to record the tests from the bottom of the samples.

2.1.1 Design requirements

According to the literature review, the bonding strength between PDMS and other materials (glass, gold, PDMS, among others) depends on various factors, such as the material, layer thickness, and bonding process. Different articles report the leakage pressure of PDMS bonding tests; for example, PDMS bonded to PDMS can achieve a bonding strength higher than 500 kPa [58]. On the other hand, PDMS and gold bonding strength can reach 250 kPa, without functionalization processes; PDMS bonded to PS reaches leak pressures of 800 kPa. The force sensor selected for this measuring system must detect forces applied on a specific area that corresponds to the pressures reported in the literature. A resolution of 50 kPa can be enough for this system.

On this work, gold samples coated with PDMS will be used to test the performance of the measuring system in SPR-based sensors, these samples are described later. Therefore, the proposal system must measure forces on a small area (circle of 1 mm diameter) where the gold sample was drilled.

2.1.2 Measuring system architecture

The instrument is separated into four different stages, as shown in Figure 10. The first one is the excitation stage, in which the mechanism transports the deflection force from the polymer membrane to the force sensor, and adds adequate force offset to the sensor. By adding a proper offset, the system will avoid errors due to the start of the contact between the mechanical parts.

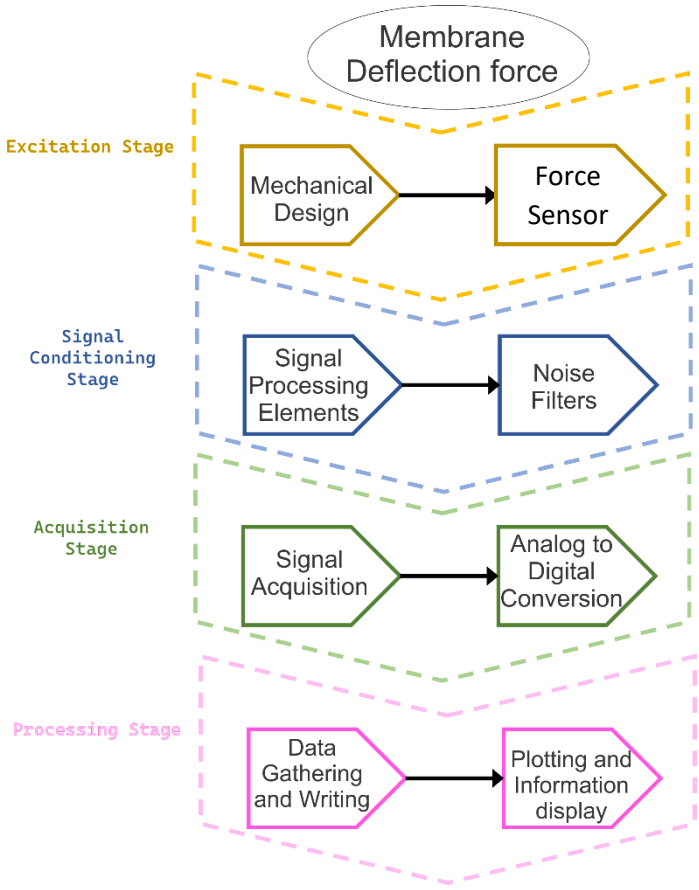

Figure 10 System architecture

In the second stage, the signal is conditioned, which oversees the correct signal processing in two ways: first, it adds an operational amplifier (OPAMP) working on inverter

mode to linearize the input voltage; second, it uses passive filters, such as capacitors, which filter noise signals originated from the power supply elements and background signals. At the end of this stage, the signal obtained is an analog voltage output ranging from 0 to5 V.

In the third stage data is acquired and converted; the voltage produced in the last stage is treated to convert it into a digital value. This operation is carried out by a microcontroller (Arduino Uno), which has an analog to digital converter of 10 bits. Finally, the digital parameters are printed in the serial port as ASCII characters after the analog to digital signal conversion.

In the last stage data are processed, in which the data obtained in the past stage is now ordered and gathered in a text file. The data is arranged and processed in the Origin software using a Python script to obtain the needed information.

2.2 Mechanical design

The mechanical system is based on the cylinder-plunger mechanism. When a force is applied to the top of the plunger, it transports the force to the tip of the cylinder, as shown in Figure 11 a). Using a spring will make the system more stable and endow a force offset, which is needed to ensure the linear behavior of the piezoresistive sensor (on a limited range of operation). Figure 11 b) shows the desired and simplified system, in which the sensor is attached to the ground, and it will measure the force in the tip of the system, the sensor at the end will measure the force due to the changes on the layer and the system.

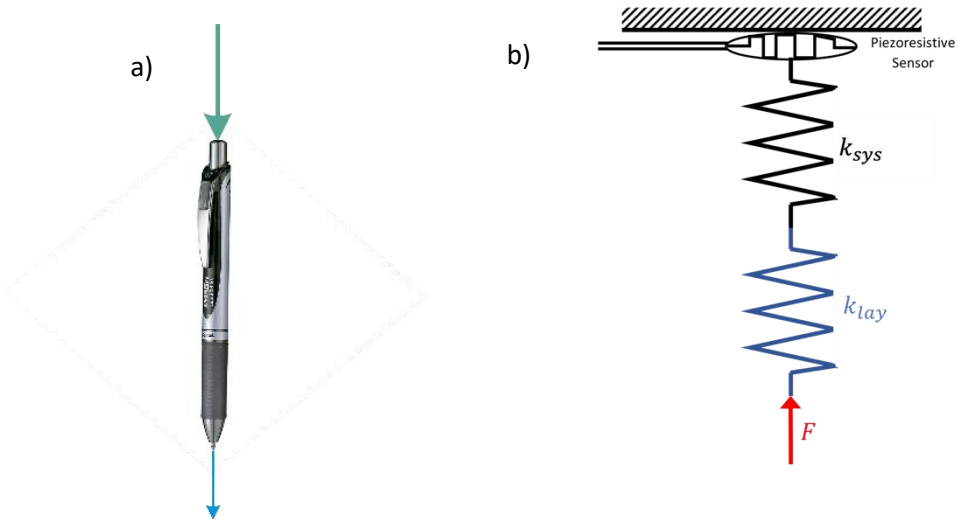

Figure 11: a) Cylinder-plunger system (pen); b) System simplified model.

The mechanical system shown in Figure 12 consists of four main elements: a) the piezoresistive sensor base, which is the element attached to the ground and holds the sensor; b) the base, which contains the plunger and the spring; and the needle, which contacts the polymer layer; c) the plunger, which transports the applied forces on the top of the pen to the pin; d) the spring, which brings an offset to the piezoresistive sensor and makes the system more stable to small vibrations; e) the complementary base, which is attached to the base and the tip of the spring; f) needle, is the element which applies the transmitted force to the membranes.

The base and the plunger were manufactured using the Vat Photopolymerization process. This allows a good resolution and a smooth surface finish, which is important because the piezoresistive sensor is sensitive to constant surface contact. The friction between the plunger and the base also affects the sensor. It is important to notice that these smooth finish surfaces cannot be enhanced by using other available additive manufacturing processes at the same cost.

Some considerations taken in the mechanical design were influenced by using the piezoresistive sensor, according to the datasheet and the guide provided by the sensor's manufacturer.

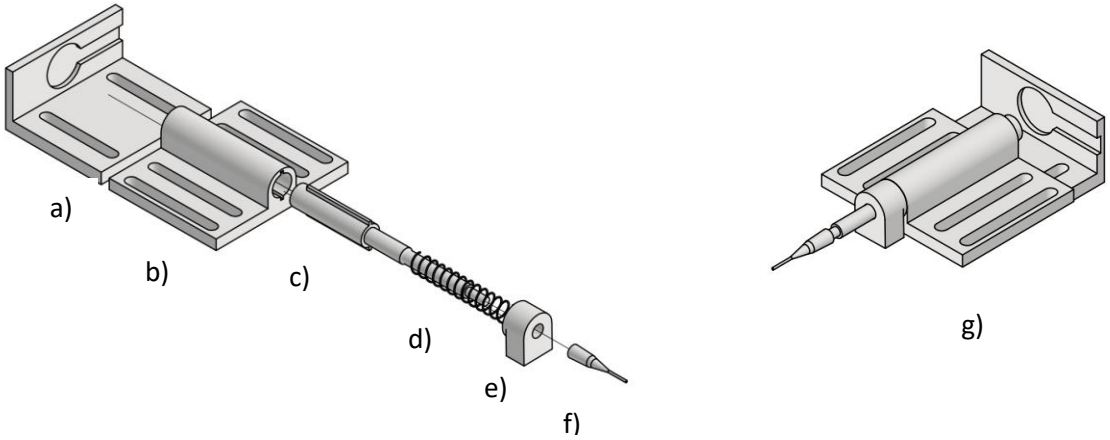

Figure 12 Main mechanical design: a) piezoresistive sensor; b) base; c) plunger; d) spring; e) complementary base; f) needle; and g) system assembled.

2.2.1 Sample holder

The measuring system uses a micrometer to displace the samples from the initial position to the desired final position; the micrometer was coupled to a stepper motor to automate the transportation process.

A sample holder base (Figure 13) has been designed to fix the samples to the micrometer and ensure that both have the same displacement. This sample holder is formed by a printed base with a hole in the center to allow the needle to go through it; two

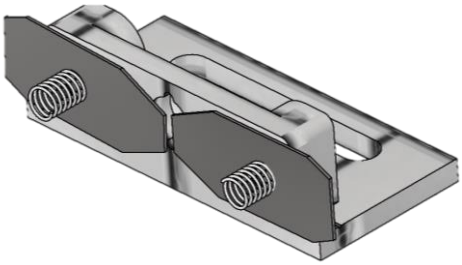

Figure 13 Sample holder

springs that apply the needed force to attach the metallic sample to the base, and finally two metallic sheets to hold the metallic surface.

The main problem with the coupling between micrometer and the stepper motor was that a variation on the micrometer's dial changed the vertical position of the micrometer axis. To ensure contact between the two axes a compressible base for the stepper motor was designed, Figure 14. This is formed by two triangular printed bases where

the motor is placed, then three springs with screws to self-adjust the height of the motor. On Appendix D the electrical circuit for the motor is shown.

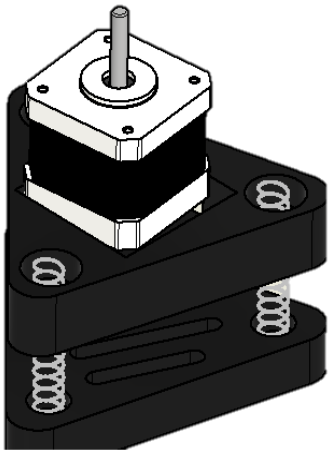

Figure 14 Stepper motor base to follow the micrometer axis.

2.3 Circuit design

2.3.1 Sensor

A piezoresistive sensor has been selected because it is widely used to measure force and pressure. Some properties of piezoresistive sensors, such as their low cost, wide range, and resolution, make them a suitable option among existing force and pressure sensors. There is a difference between the contact area of the membrane (circle of 1 mm diameter) and the piezoresistive active area (circle of 14 mm diameter). A mechanical system was designed to ensure that both surfaces constantly contact each other to account for this difference.

The piezoresistive sensor, FSR 402 from Interlink electronics, is shown in Figure 15. It was selected due to its range, sensitivity, and relative low drift. The variation in the applied force in this sensor is reflected in resistivity changes. According to the technical datasheet, the resistivity can change between 0 and 10 MΩ. In addition, the range of forces is between 0 and 5 kg, with actuation forces of less than 20 g. Finally, the drift of the sensor is less than 5% per 35 days. In Appendix the values, the key dimensions, and main features are shown.

Figure 15 Piezoresistive sensor FSR402

2.3.2 Signal process circuit

Three different arrays of amplifier circuits were studied: the voltage divider with an OPAMP, the Wheatstone Bridge with an OPAMP, and an OPAMP working on the inverter mode (current to voltage converter). Figure 16 shows the output for Wheatstone bridge circuit compared to the voltage inverter configuration, both have a similar trend, however, the sensitivity is slightly higher on the inverter voltage circuit; moreover, with this offset and the increments tested, the Wheatstone bridge output is saturated in 60 grams.

From these arrays, the best option was the OPAMP on the inverter mode Figure 17, which has a linear response in a range of forces applied. Results from the Wheatstone bridge array showed a decrease in the sensitivity of the device, this could be attributed to the selection of resistors for this array. The response of the circuit shown in Figure 17 can be calibrated by varying the gain resistance in the circuit, which were decisive factors when using this array. With the appropriate resistors, the final output varied between 0 V and 4.5 V.

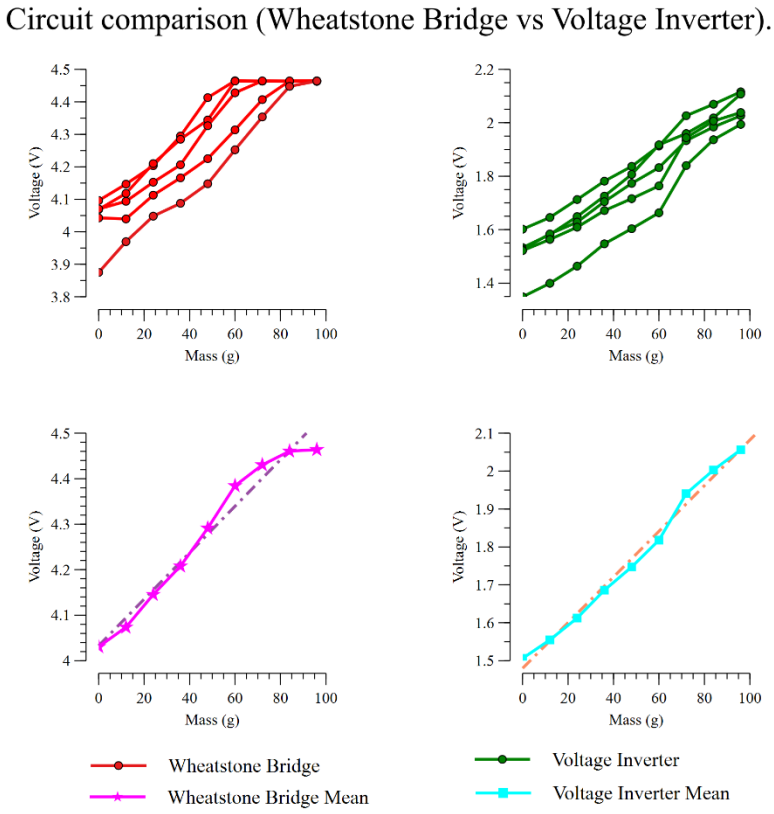

Figure 16 Circuit comparison between Wheatstone bridge and Voltage inverter.

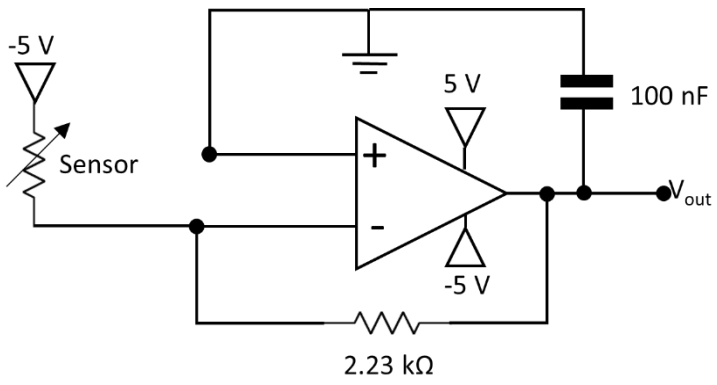

Figure 17 Current to voltage converter

2.3.3 Data acquisition and processing

The circuit's final output is an analog voltage signal converted to a digital value by a microcontroller Arduino Uno. To perform this task this microcontroller has a 10 bits Analog to Digital Converter, which can divide 5 V into 1023 threshold levels. These levels are important because they define the resolution of the system.

A python script gathered all the data and wrote it into a text file. This information was treated using Origin pro in two steps: first, by plotting the data, and second by obtaining a linear regression applying the least square regression method.

2.3.4 Programming.

The program to run the test on the measuring system is depicted in Figure 18.

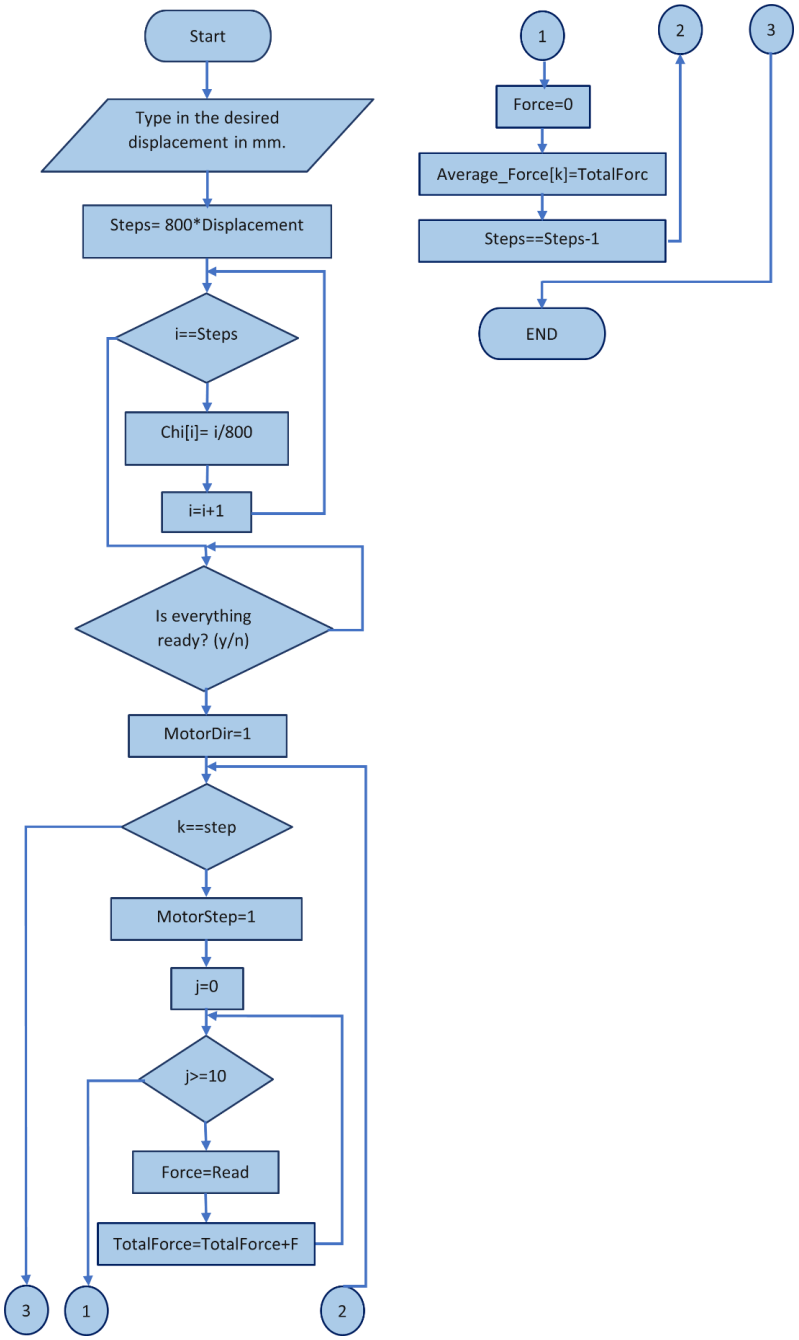

Figure 18 Program flowchart to obtain the force and deflection

This program starts by asking the desired displacement for the test, then it calculates the steps that the motor needs to complete that displacement, as follows:

$$Steps = Displacement * \alpha \quad (30)$$

where α is the constant that relates the steps taken by the motor and the displacement traveled by the sample. The micrometer employed has a resolution of 0.25 mm per turn and the stepper motor performs a turn in 200 steps, then constant α can be calculated as:

$$\alpha = \frac{200}{0.25}\left[\frac{Steps}{mm}\right] = 800\left[\frac{Steps}{mm}\right]$$

The program converts the displacement input into the number of steps and calculates a deflection vector in millimeters. In addition, the program asks the user to check the sample positioning to start the program. If everything is ready, the motor will take a step and measure 10 values of the sensor, after which the average force will be stored in the force vector. Finally, when the motor finishes all the steps, the force and displacement vectors are plotted, and the raw data is printed on a text file.

2.4 Final setup

The Integration of all the mechanical parts is shown in Figure 19 a), the mechanical design and the micrometer are attached to an optical table to reduce vibrational noise. Additionally, Figure 19 b) shows the exploded view of these parts, to show where the needle will contact the gold samples.

The final system is depicted in Figure 20. The motor base was placed on an optical table to reduce vibration noise or other mechanical interference. The main mechanical system, a), and the micrometer with the sample holder, b), were attached to a vertical rail to align the needle of the system to the sample holder. The micrometer was coupled with the stepper motor by using the stepper motor base, c), and an additive manufactured couple for the axis. During the test, the sample was placed, d). Before performing the tests, the alignment of needle-sample was verified with a camera.

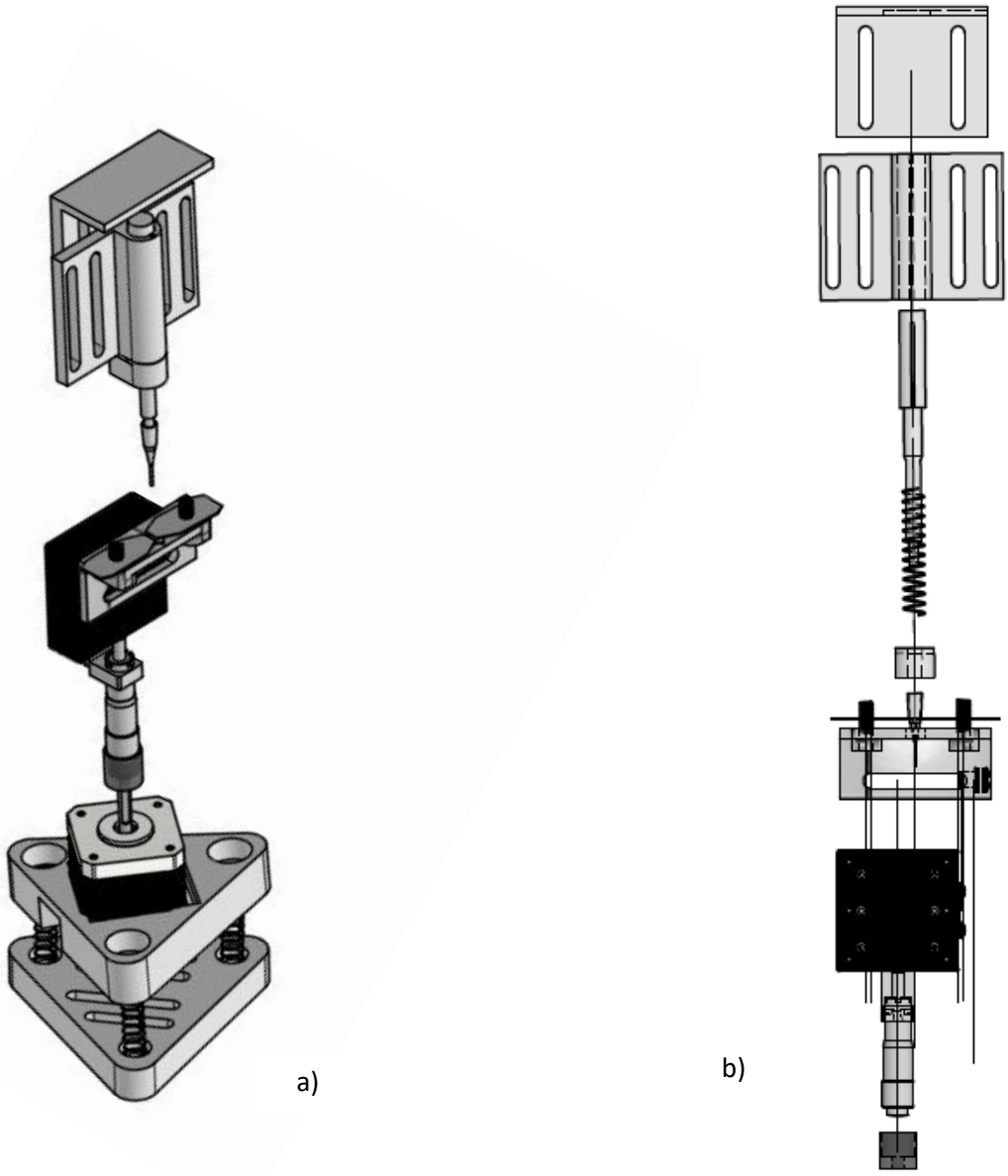

Figure 19 a) Final setup of the measuring system; b) exploded view of the measuring system

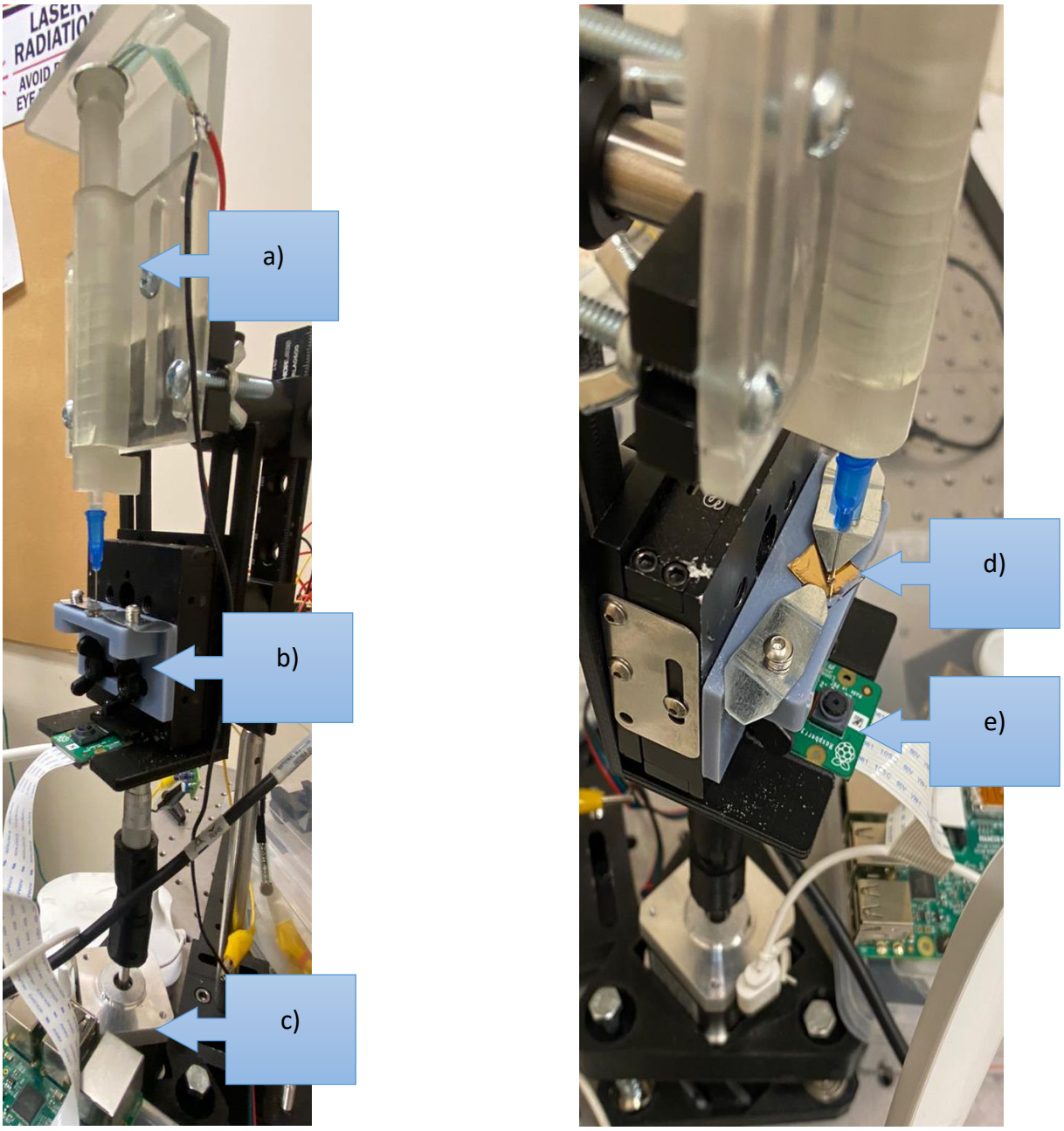

Figure 20 Final setup of the measuring system: a) Main mechanical system; b) Sample holder and micrometer; c) Stepper motor on the motor base; d) Gold Sample position during a test and e) Video camera connected to a Raspberry Pi.

2.5 Calibration

Tests were run to obtain the calibration data, and subsequently, the data were processed to plot a calibration curve. The system parameters, such as sensibility, reproducibility and error were calculated based on the calibration curve. The system was

set up with the FSR sensor attached to the bottom, by doing this the system can be calibrated using pre weight objects with a scale.

This instrument measures forces applied on a small surface (flat needle of 0.8 mm diameter), and by using a micrometer with a resolution of 0.01 mm, the system also measures the total deflection of the membrane. Operation ranges are based on the literature[69] [70], the maximum operating pressure of SPR sensors ranges from 10 to 20 psi, and the deflection expected range for the PDMS is between 1 mm and 1.5 mm.

The calibration process was performed in two steps. First, the sensor was set up mechanically by compressing the spring to a known displacement; this compression is the offset force applied to the piezoresistive sensor (Figure 21). Second, by varying the weight directly applied to the needle, the output voltage was read by the microcontroller (Arduino Uno).

Figure 21 Calibration setup.

The calibration curve was generated by varying the weight from 0 to 180 g with 20 g increments Tests were made by quadruplicate and results are shown in Figure 22 a. This information allowed obtaining the mean and the standard deviation as shown in Figure 22 b. Based on the information obtained from the calibration curve, the linear relationship between voltage and force through the method of least squares was

obtained. This process overcomes random errors and allows obtaining the intercept and the slope. The least squares method can be summarized by the expressions:

$$A = \frac{\sum E \sum s^2 - \sum s \sum sE}{k \sum s^2 - (\sum s)^2} \quad 31$$

$$B = \frac{k \sum sE - \sum s \sum E}{k \sum s^2 - (\sum s)^2} \quad 32$$

where the constant A is the intercept and B represent the slope of the linear function, k is the number of readings, E are the output values and s are the input values [23].

Table 1 shows the values of the four calibration tests that were taken under similar conditions.

Table 1 Calibration data and mean.

Mass (g)	Test 1 (V)	Test 2 (V)	Test 3 (V)	Test 4 (V)	Mean (V)
0	2.361183	2.421291	2.350099	2.345312	2.369471
20	2.472901	2.487842	2.453467	2.427247	2.460364
40	2.611181	2.533545	2.546435	2.585645	2.569202
60	2.687696	2.654053	2.672656	2.612206	2.656653
80	2.882812	2.826366	2.897607	3.017236	2.906005
100	3.186036	3.087697	3.112012	3.176366	3.140528
120	3.341066	3.083253	3.070362	3.123243	3.154481
140	2.784668	3.465773	3.485694	3.508741	3.311219
160	3.560205	3.587843	3.590137	3.623145	3.590333
180	3.659619	3.727734	3.760644	3.748925	3.724231

After applying equations 31 and 32 to the data in the Table 1, the linear regression for the mean column, the intercept value A and the slope B are:

$$A = 2.291681091$$

$$B = 0.007739621$$

The expression that relates the voltage and the force is:

$$V = 2.29 + 0.00774 * F \quad (33)$$

Figure 22 a) shows the linear regression is plotted along with the scattered data of the voltage mean from Table 1, and Figure 22 b shows the calibration curves obtained under similar conditions.

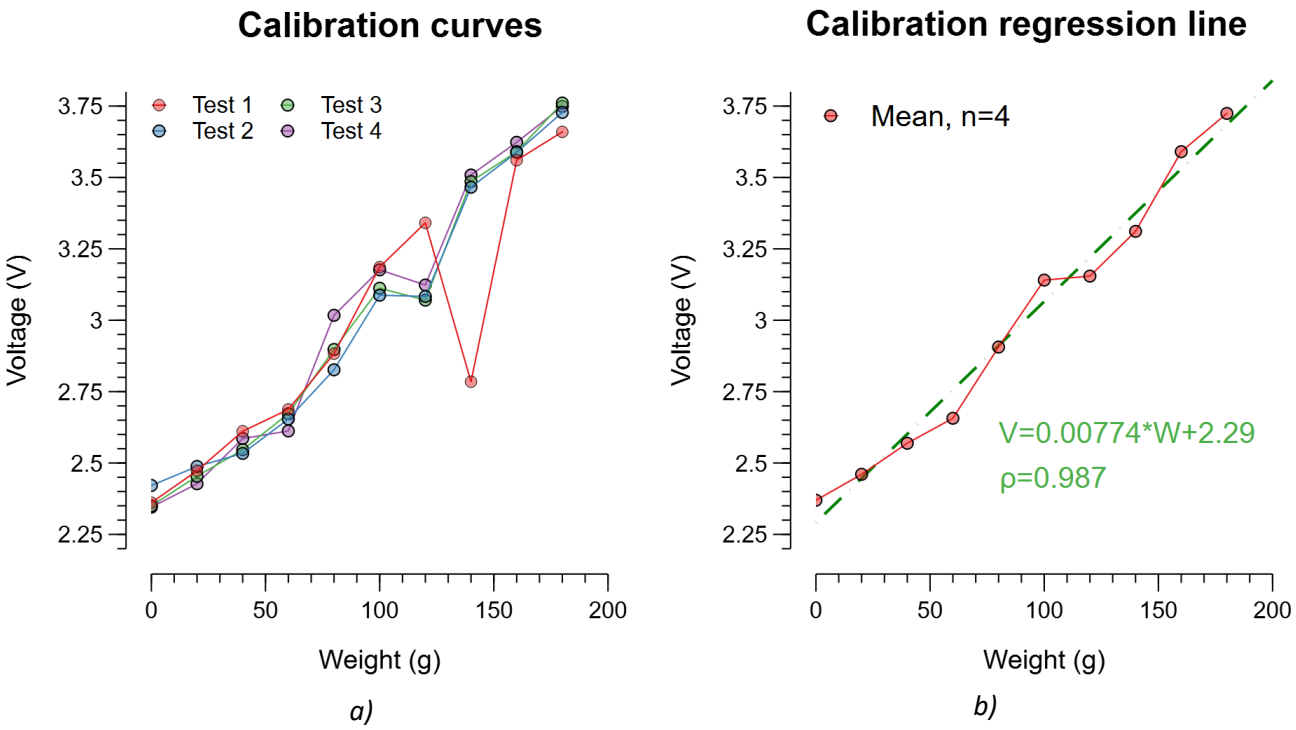

Figure 22 Calibration curve a) Calibration curve with mean and standard deviation, n=4, b) 4 tests varying weight.

2.6 Sample preparation

Figure 23 shows the process used for producing the two functionalization processes compared in this work. First, glass slides coated with a gold layer of 100 nm were used. These slides were drilled into a 1 mm diameter hole in the center. Second, all the samples were rinsed with acetone, isopropanol, and deionized water. After that, the samples were divided into two main groups, namely: the reference group and functionalized group. Samples from the latter group were immersed in a MPTMS and ethanol solution to modify the gold surface, and thus the bonding strength with PDMS. Then, both groups were spin coated with PDMS 184 Sylgard and the PDMS cured on a hotplate at 125 °C for 10 minutes and then 70 °C for 30 minutes. According to Johnston et al, 2014, the Young's modulus for curing at 125 °C is $2.46 \pm 0.16\ MPa$, and the ultimate

tensile strength is $7.65 \pm 0.27\ MPa$. These values help as comparison, however, the curing time for the PDMS was reported as 48 hours; in contrast, the curing time for this process was significantly shorter, 24 hours. Additional to this functionalization (MPTMS), another functionalization process was tested, 11MUA. The same process of Figure 23 was followed, only changing the MPTMS for 11MUA.

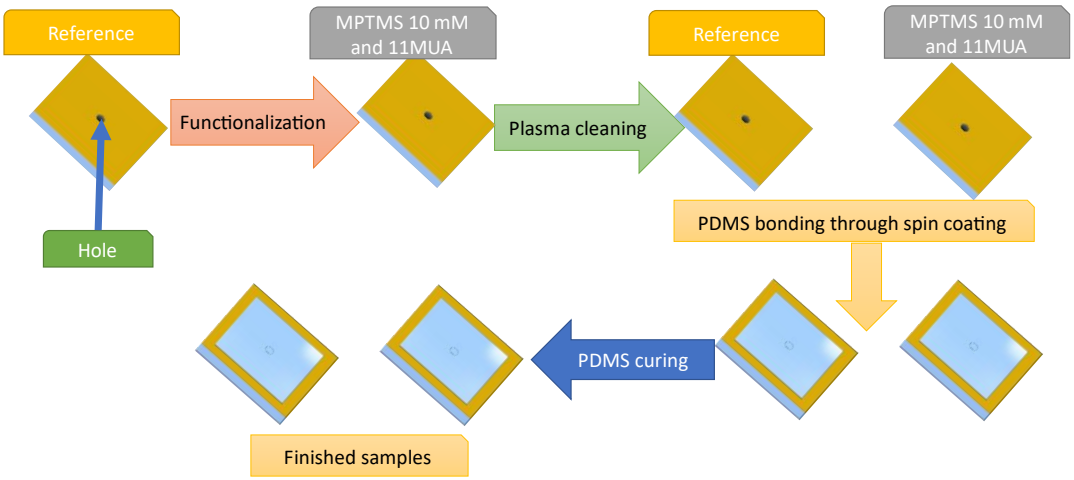

Figure 23 Gold sample preparation process, for functionalization and reference samples.

3

RESULTS AND DISCUSSION

3.1 Sensor estimated cost

An estimated cost for this measuring system is depicted in Table 2, the main parts are included in the final setup of Figure 20. The costs of building elements with the Vat photopolymerization and the Material Extrusion machines were calculated according to the Anycubic software, Workshop, this shows the material and time needed to built them. FSR sensor and electronic elements were acquired on Digikey Canada.

Table 2 Estimated cost for the measuring system

Element	Number of parts	Consume material	Time	Cost (USD)
Sensor base	1	22.385 ml	2h	1.119
Base complement	1	2.5 ml	20 min	0.67
Plunger	1	5.565 ml	1:30 h	1.22
Base	1	26.312 ml	5 h	5.789
Motor base	2	60 ml	4 h	15
Camera support	1	12.062 ml	37 min	2.658
Springs	6	N/A	N/A	10.92
Raspberry Camera	1	N/A	N/A	13.65
Stepper motor	1	N/A	N/A	30
FSR sensor	1	N/A	N/A	12
Total				**93.026**

3.2 Part I: Sensor characteristics

It is important to calculate the static characteristics of a sensor because it allows describing the sensor behavior and reliability of its measurements.

3.2.1 Sensitivity

By using the linear regression of equation 33 and the calibration curve of Figure 22 b), the sensitivity is represented by the slope of the linear regression, this is:

$$S = 0.00774\left(\frac{V}{g}\right) \quad 34$$

3.2.2 Residual error:

Residual errors were obtained in Table 3 by applying equation 25 to the data from the linear fitting and the measured values. With the information from Table 3, a residual error scattering plot was obtained (Figure 24) to analyze the relationship between the error and the independent variable.

The independence of residuals and the independent variable is crucial, because if we can establish a relationship between these variables, then the linear regression is not adequate for the system described in system [71]. An outlier is a data point that is quite distant from the surrounding values, a way to determine if a value is an outlier is presented by Shardt, 2015; this method is depicted in the equation below:

$$Z_i = \frac{x_i - \bar{x}}{\sigma} \quad 35$$

Equation 35, also known as the 3s rule, establish that the value should be considered as outlier if the error is at least three times standard deviation, in other words, Z_i is equal or higher than three [71]. Additionally, an outlier can be identified by a visual test, for instance, in Figure 22 a) the test number 1, shows a different behavior compared to the other tests; therefore, this point can be considered as an outlier, and this was confirmed by the 3s rule.

$$Z_8 = \frac{63.91 - 131.94}{45} = 3.008 \quad 36$$

Outliers can be originated by human errors during the measurements.

3.2.3 Accuracy:

The accuracy was calculated according to equation 28, and the information from Table 3.Table 4 presents all the accuracy values, it is observed that the lowest accuracy in the measurements is 60 grams with 79 % of accuracy, and the highest value registered is 99.5% which corresponds to a weight of 80 grams.60 grams points are observed on Figure 24, all of them have a positive error; additionally, show the same behavior on Figure 22 a). One explanation of this can be a systematic error, which can

be attributed to an error of an element, for example the friction between the plunger and the base.

Table 3 Calibration residual error

Desired Value (g)	W1 (g)	W2 (g)	W3 (g)	W4 (g)	Mean (g)	Error_1 (g)	Error_2 (g)	Error_3 (g)	Error_4 (g)
0	9.20	16.96	7.76	7.15	10.27	-9.20	-16.96	-7.76	-7.15
20	23.63	25.56	21.12	17.73	22.01	-4.28	-6.21	-1.77	1.62
40	41.50	31.47	33.13	38.20	36.07	-1.50	8.53	6.87	1.80
60	51.38	47.04	49.44	41.63	47.37	9.26	13.61	11.21	19.02
80	76.59	69.30	78.50	93.96	79.59	4.70	11.99	2.79	-12.67
100	115.77	103.06	106.20	114.52	109.89	-13.83	-1.12	-4.27	-12.58
120	135.80	102.49	100.82	107.65	111.69	-13.21	20.10	21.76	14.93
140	63.91	151.91	154.48	157.46	131.94	79.32	-8.68	-11.25	-14.23
160	164.11	167.68	167.98	172.24	168.00	-0.23	-3.80	-4.10	-8.36
180	176.95	185.75	190.01	188.49	185.30	7.57	-1.23	-5.48	-3.97

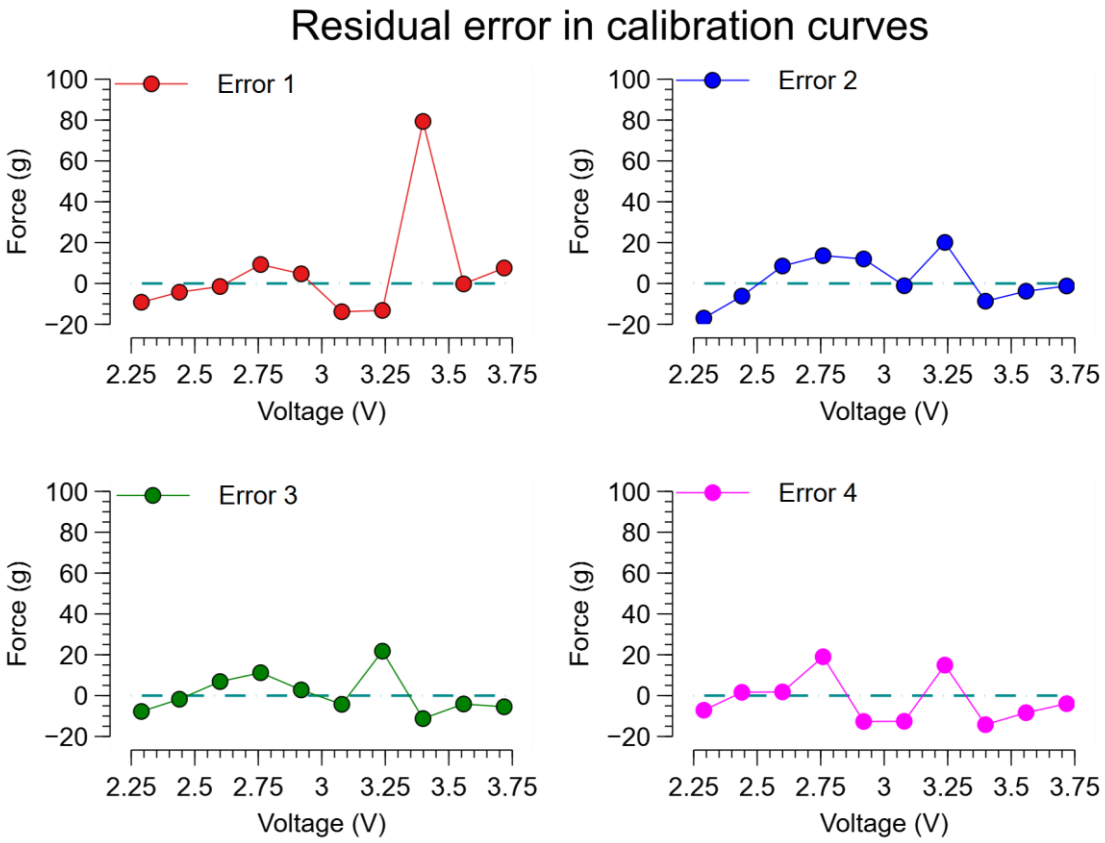

Figure 24 Residual error of each calibration curve.

Table 4 Error and Accuracy

Voltage (V)	Mean value (g)	Error (%)	Accuracy (%)
2.29	**10.3**	-	-
2.4398	**22.0**	10.1	89.9
2.5996	**36.1**	9.8	90.2
2.7594	**47.4**	21.0	79.0
2.9192	**79.6**	0.5	99.5
3.079	**109.9**	9.9	90.1
3.2388	**111.7**	6.9	93.1
3.3986	**131.9**	5.8	94.2
3.5584	**168.0**	5.0	95.0
3.7182	**185.3**	2.9	97.1

3.2.4 Precision

The following glass sample was tested four times before breaking off. Figure 25. shows the system output returning almost to the same position the first three times until the breaking off point. These results were corroborated by using equation 29, repeatability or precision on the first four tests; the average of these graphics was calculated, and the precision for each point was calculated using equation 29. The lowest and highest precision value for each graphic is shown in Table 5.

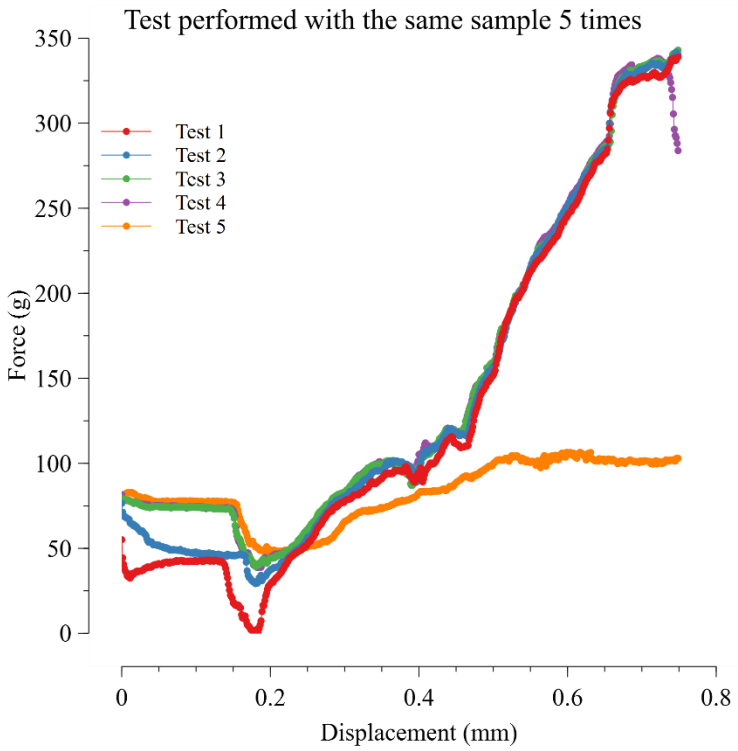

Figure 25 Same glass sample over 5 runs (T4 membrane breaking, T5 last run without PDMS membrane).

Table 5 Precision on the same glass sample 4 times

Precision	Test 1	Test 2	Test 3	Test 4
Minimum	0.704	0.895	0.84	0.822
Maximum	0.999	0.999	0.999	0.999

The same equation (equation 29) was used to obtain precision of the calibration curves from Figure 22 a). Precision values were obtained for each point and for all the tests, Figure 26 shows the precision for each calibration point. This plot depicts that the four tests showed a low precision value on the first calibration point (0g). Another point with a low precision value is present in the calibration test 1 (red line), which is consistent with the error data from Figure 24, this point is where the outlier is present. Overall, most of the precision values are higher than 0.8 or 80% of precision for measuring the same inputs.

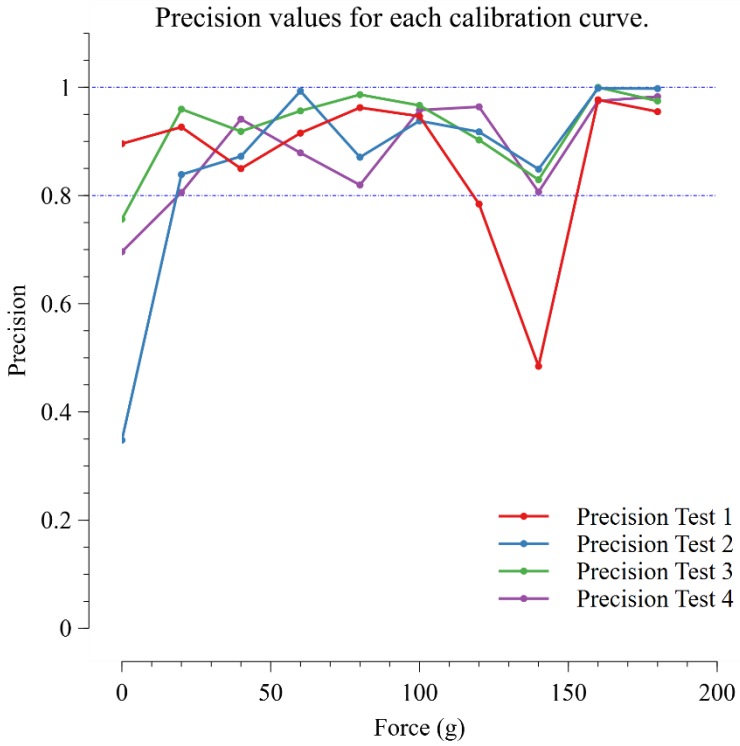

Figure 26 Precision values obtained for each calibration curves.

3.2.5 Resolution

The resolution of the system is defined by using the calibration curve (Figure 22) with increments of 20 g. However, the datasheet of the sensors indicates that 15 g is the minimum force needed to obtain a change in the resistance.

3.3 Part II: System response to gold samples

Before testing the system with gold samples, many tests were run to analyze the response of the system. Glass samples were evaluated under similar conditions instead of using the gold samples. These were prepared with the same process as depicted in Figure 23.

3.3.1 Response of the system with glass-PDMS samples.

The system was tested several times with different samples. The first readings showed the system's response when the PDMS membrane is not present on the glass.

Figure 27 shows the behavior of two glass samples, the first one (black line) with a PDMS membrane, and the second one without a PDMS membrane (red line). In this picture, we can identify that the sample without a membrane behaves like a horizontal line because the sensor does not measure any force applied on the tip of the plunger. The behavior of the red line shown in Figure 27, can be attributed to the bonding strength of the sample; first, the PDMS layer is touched by the needle at 0.5 mm, then the force applied increases until the PDMS is broken at 0.9 mm of displacement; after breaking, the graphic returns almost to the same value. Some peaks and steady values can be attributed to systematic errors, for instance, the friction of the mechanical system.

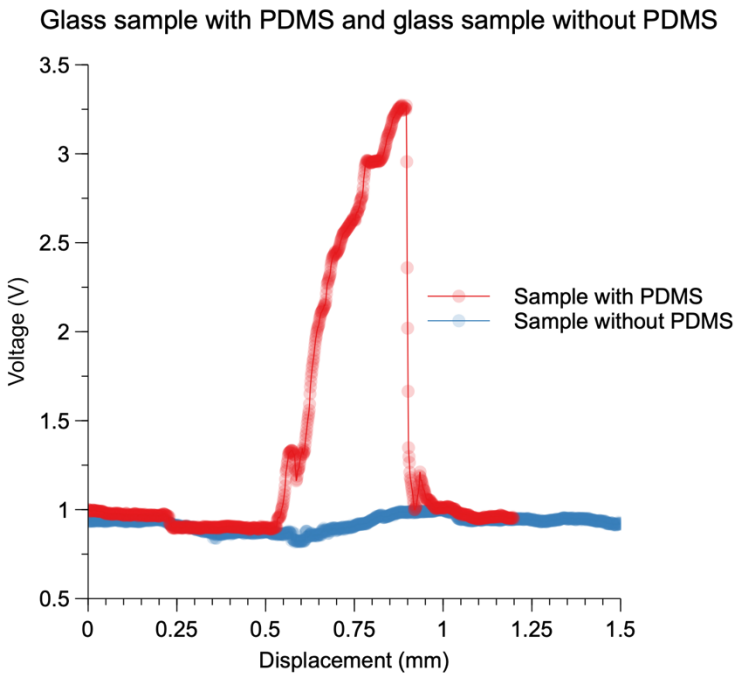

Figure 27 System response to glass sample with and without PDMS membrane.

3.3.2 Constant surface contact

After the last tests, the deflection for the next tests was settled from 0 to 1.5 mm. This range ensures that all the samples will reach the breaking-off point. Figure 28

shows the behavior of three different samples, displaying an unexpected behavior of the slopes within the first 0.6 mm and in the 0.8 mm. Zoom to these peaks, displays a decay in voltage that represents a decay in force.

According to the Interlink Electronics guide [72], the contact area must be constant. On the contrary, this can cause variations in the output voltage due to the uneven force applied to the sensor. Moreover, this guide emphasizes the importance of an appropriate offset for the sensor. The irregularities observed in both Figure 27 and Figure 28, kept showing in the next tests. After a deep analysis of the system, we observed that the plunger was off centered to the base. This is the reason why the contact area was irregular, and according to the sensor manufacturer, to ensure acquired force measurements the contact area must be consistent and within the sensor's active area (a circle of 14 mm diameter).

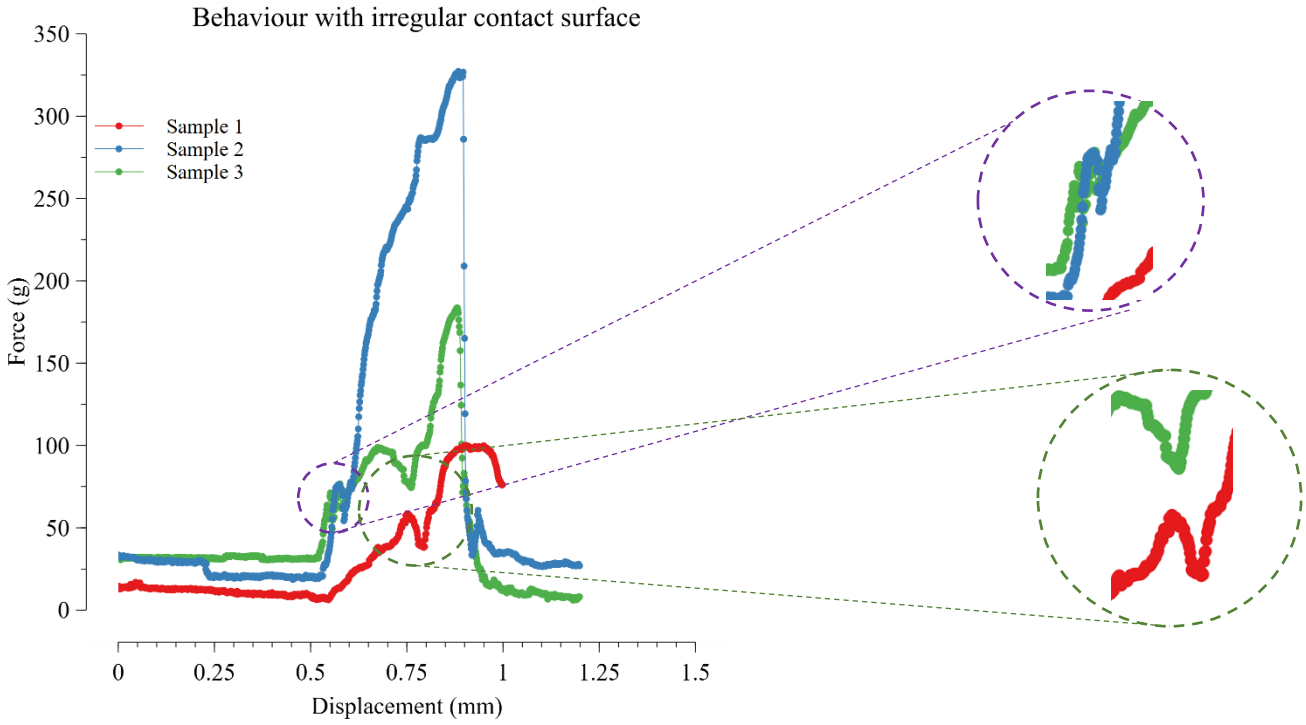

Figure 28 Behavior due to irregular contact surface.

3.3.3 Signal saturation.

Other samples were aligned, but a different behavior was observed, for example, an abrupt increase in the voltage, saturating the output through the entire test, as shown

in Figure 29. This behavior is attributed to an alignment error because the needle touches the gold, and the sensor reaches its maximum output.

Considering that this problem would repeat in the future, the use of a video camera was implemented. With this camera, the user can see on a monitor in real-time the sample from the bottom, which allows ensuring a good alignment and proceed to run the test.

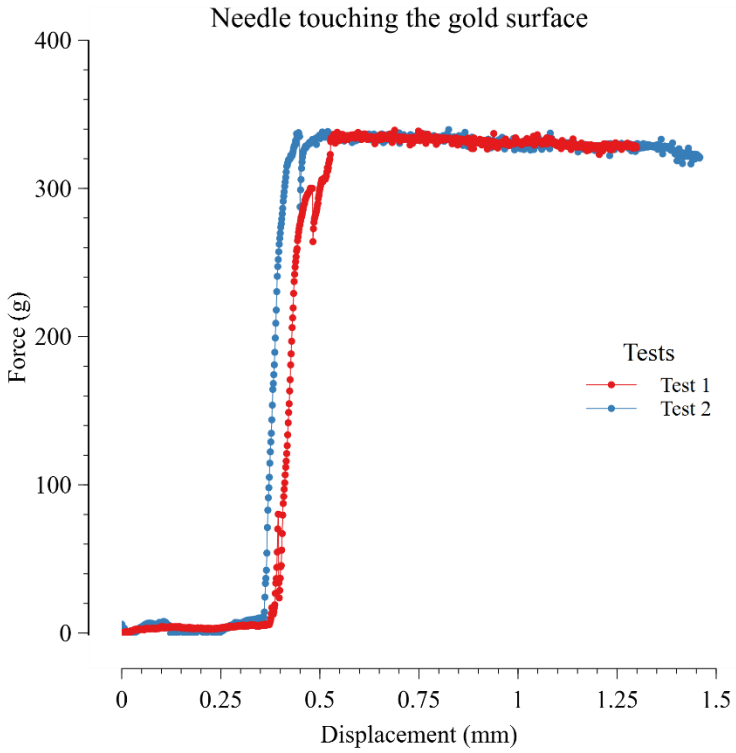

Figure 29 Signal saturation example

3.3.4 Reference samples

After solving the previous problems, reference samples were evaluated under the same conditions and the same offset force. We used the calibration curve previously obtained to convert the voltage output to force in grams. Figure 30 a) shows the complete test, and it is observed that all the samples finish with a little force applied to them. Figure 30 b) shows the system's behavior before breaking off, as we can see, the reference samples 1 and 3 have the same trend.

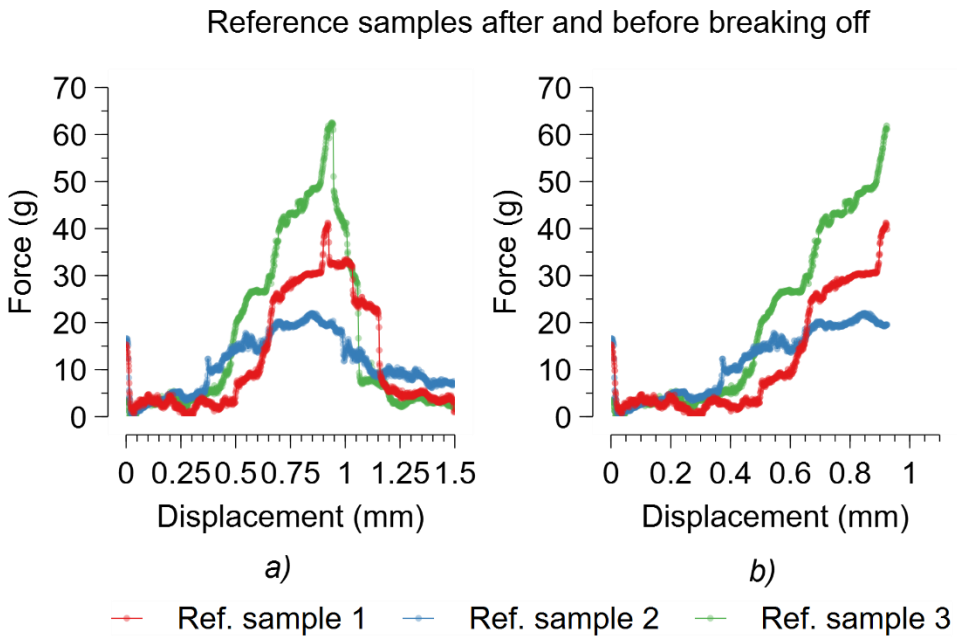

Figure 30 Reference samples: a) complete behavior; b) before breaking off.

3.3.5 11MUA samples

11MUA samples were evaluated under the same conditions as the previous samples. Figure 31 a) shows the behavior of the samples before the breaking-off point. These results do not show significant similarities in the slope between them. On the other hand, samples 1 and 2 present the same breaking point. Additionally, after the breaking point of sample 3, the output does not return to the same value, which can be interpreted as a force applied to the system. Finally, 11MUA results were not consistent with each other. This can be attributed to lack of strong in the chemical bonds between PDMS and 11MUA presented by some authors (Byun et al, 2013); additionally, a bad functionalization process, or non-uniformity on the substrate layer can cause this inconsistency [66].

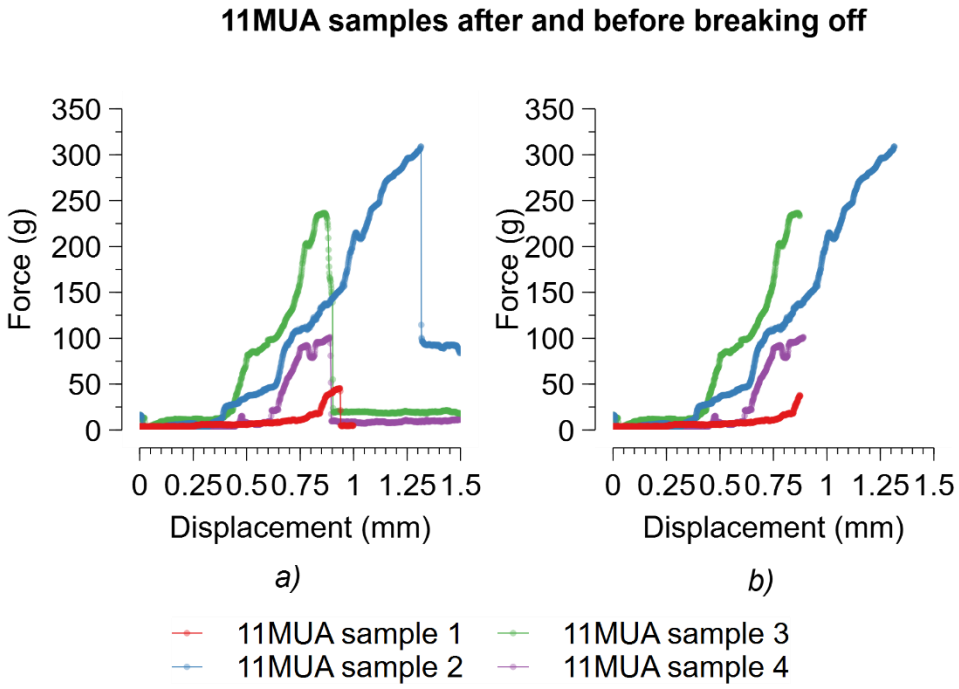

Figure 31 11MUA samples: a) Complete test; b) Before breaking off.

3.3.6 MPTMS samples

Figure 32 a) shows MPTMS results from the complete test, in which it is observed that the output after the breaking-off point is higher in some samples, compared with reference samples and 11MUA samples. A possible explanation is the increases on PDMS stiffness after MPTMS functionalization that was reported by Osmani et al, 2016. Figure 32 allows to compare only the slopes. It is important to note that some samples have the same breaking-off point and slope tendency. These results are similar between them, according to Byun et al, 2013, MPTMS liquid treatment has a better adsorption, despite the non-uniformity of the gold surface it increased the bonding strength.

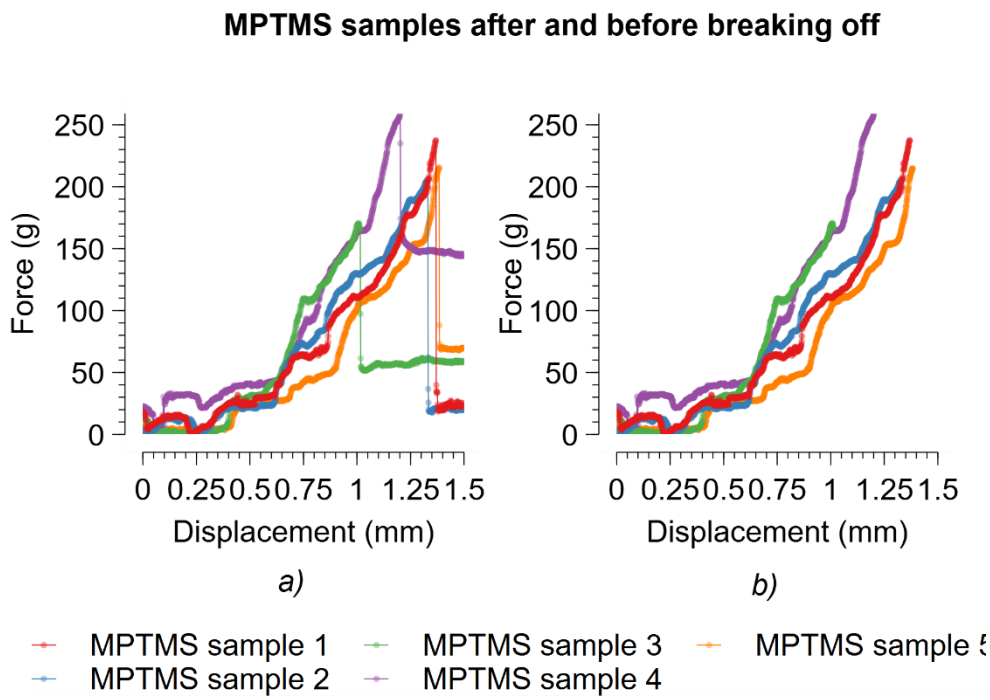

Figure 32 MPTMS samples: a) Complete test; b) Before breaking off

3.3.7 Comparison between Reference and MPTMS

A comparison between reference and MPTMS samples is shown in Figure 33. First, on a) the output forces after breaking off point on the MPTMS samples are stronger than the output forces on the reference samples; As it was mentioned before, the sample preparation process was the same for both groups, only differ on the chemical treatment. Second, on Figure 33 b), the slopes on MPTMS samples are higher than the slopes on reference samples. Finally, the maximum forces are significantly stronger, compared to the ones that reference samples can resist before breaking off the PDMS membrane.

3.3.8 Video results

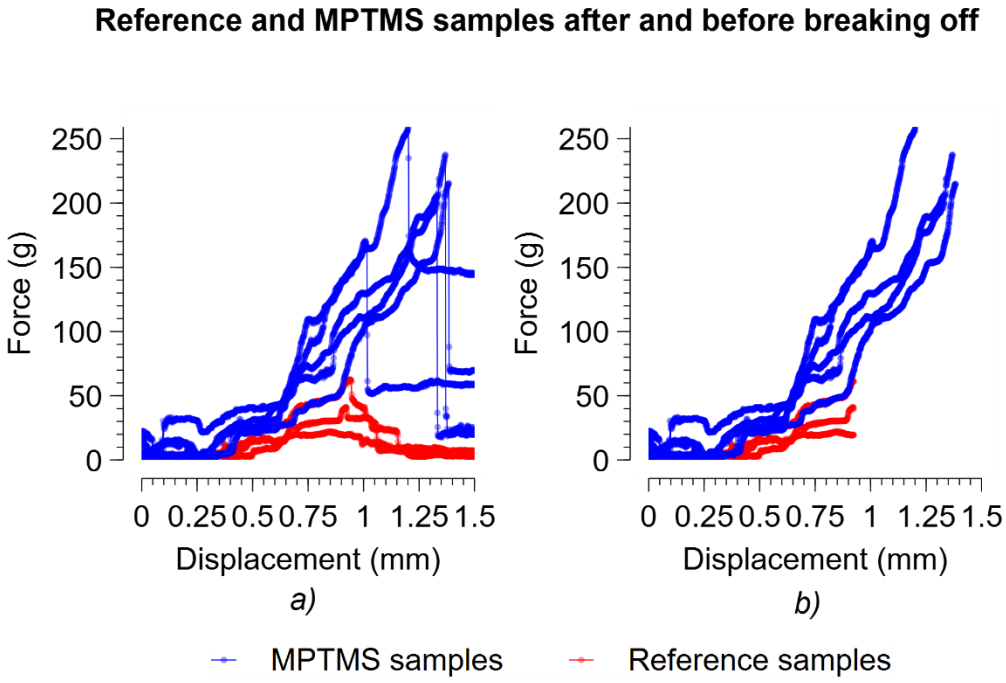

Figure 33 MPTMS vs Reference samples a) complete test; b) test before breaking-off point

By using the Raspberry Pi camera, videos of the samples before and after the breaking off point of the PDMS were recorded. These videos were projected in real time on a computer monitor to watch the test all the time. This optical resource provides a complementary information from the different testing groups.

3.3.8.1 Reference sample:

Figure 34 shows the reference sample before the breaking-off point. It cannot be observed accurately at the tip of the needle, due to the thin PDMS layer on the top of the sample. In Figure 34 b the needle is clearer because it already went through the PDMS layer. A yellow dashed circle shows the area around the needle, where the PDMS is only attached to the gold surface.

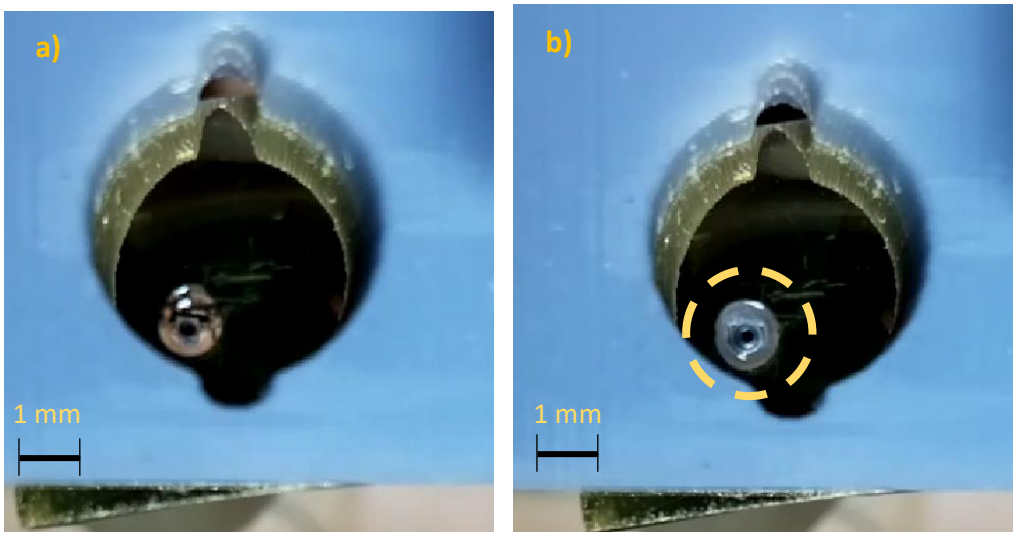

Figure 35 Reference samples a) before and b) after breaking off.

3.3.8.2 MPTMS sample:

Figure 36 shows the reference sample before the breaking-off point, this picture is a zdim image of the tip of the needle, due to the thin PDMS layer on the top of the sample. On the other hand, in Figure 36 b the yellow dashed circle shows a little glow around the needle, a difference with the previous figure, the PDMS is attached to the gold surface, and that shine might be due to the PDMS attached to the gold and the needle. This would explain the final force outputs on MPTMS samples, where the values are higher than the reference ones.

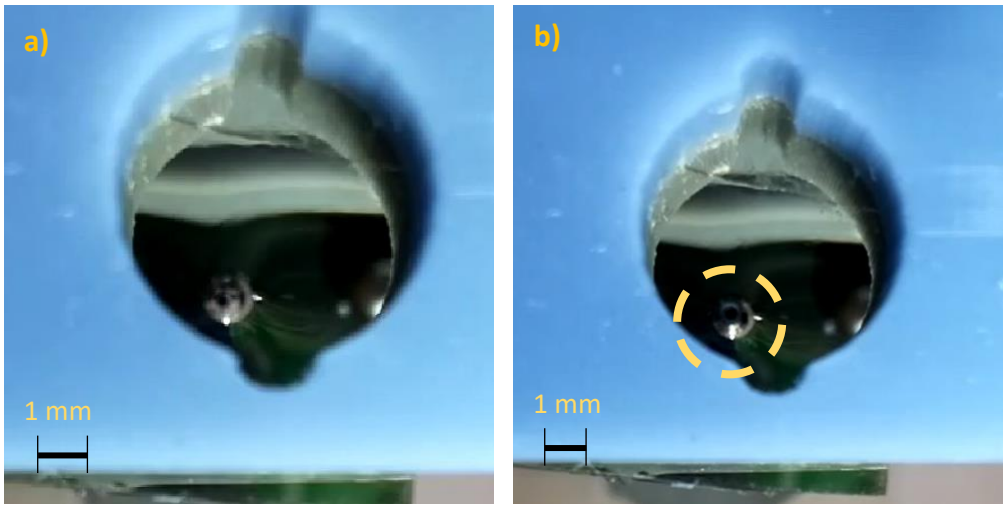

Figure 36 MPTMS samples a) before and b) after breaking off.

4

CONCLUSIONS AND FUTURE WORK

This work aimed to develop a new measuring system that measures the bonding strength between thin PDMS membranes and plasmonic surfaces. Various sensing principles were investigated to find one that fulfills the task requirements; a FSR sensor was selected due to their characteristics compared to sensors on the same price range. Two different functionalization processes were tested to modify these bonds, and based on the system response and characteristics, it can be concluded that it represents an alternative to similar current measuring systems.

A mechanical system was designed to transport the force from the bonded part to the sensor; several factors were considered based on many works done with FSR sensors, for example, a rigid and constant surface in contact with the active area, a constant room temperature during all the tests. However, further work is needed to ensure that the system works smoothly, by adding improvements to the mechanical design, so that it can help to avoid the irregular peaks observed in the results section. For small detecting areas, the tip of the mechanical system could be adapted to different testing areas, both smaller and bigger.

Rapid prototyping was used as the principal manufacturing process, allowing the system to be redesigned or upgraded easily. In addition, rapid prototyping processes have increased their use in different areas, and in recent years, have become more affordable than conventional processes. In comparison the measuring system building on this work have a cost around 100 USD, meanwhile commercially available option cost around 5000 USD. Therefore, this instrument can represent a cost-effective and

affordable alternative to measure bonding strength, compared to the current testing machines used on similar tasks.

Calibration process was performed in just in one way, which allowed us to obtain the behavior of the sensor based on weight increments. The sensor sensitivity was calculated based on the force range that the system must measure, and results showed a relatively high accuracy (lowest value of 79%), which is considered a good estimation for the force values, among the range of forces that are measured. Nevertheless, the calibration was performed by adding weights on the tip of the system, then it was turned right side up, this change can cause a systematic error, an increase or decrease on the output. Therefore, a new calibration method should be implemented to avoid this systematic error and increase the accuracy of the system.

Different sources of error were identified and addressed independently: saturation due to wrong sample position, which was repaired by using a digital camera; irregular peaks due to incorrect sensor alignment, which were treated by correcting the alignment. Additionally, residual errors were quantified to calculate the accuracy of the system. Nonetheless, as observed in previous works, the use of additional tests, like leakage test, should be considered to gain more information about the bonded area.

The plasmonic gold samples were separated into three groups, two with different functionalization methods, MPTMS and 11MUA, and the reference group. All the samples were elaborated under the same conditions and finally a PDMS membrane was added to them. From the three study groups, a remarkable difference was displayed in the system output. This difference was consistent and matches with different studies in this regard following different approaches.

Finally, based on the results presented, and the use of rapid prototyping, this measuring system proves to be a cost-effective option to measure bonding strength on plasmonic surfaces. However, many considerations must be addressed to solve systematic and gross errors highlighted in this work.

REFERENCES

1. Homola, J., Yee, S. S. & Gauglitz, G. Surface plasmon resonance sensors: review. *Sens Actuators B Chem* **54**, 3–15 (1999).

2. Wood, R. W. XLII. On a remarkable case of uneven distribution of light in a diffraction grating spectrum . *The London, Edinburgh, and Dublin Philosophical Magazine and Journal of Science* **4**, 396–402 (1902).

3. Mayer, K. M. & Hafner, J. H. Localized surface plasmon resonance sensors. *Chem Rev* **111**, 3828–3857 (2011).

4. Szunerits, S. & Boukherroub, R. Sensing using localised surface plasmon resonance sensors. *Chemical Communications* **48**, 8999–9010 (2012).

5. Duan, Q., Liu, Y., Chang, S., Chen, H. & Chen, J. H. Surface plasmonic sensors: Sensing mechanism and recent applications. *Sensors* **21**, 1–30 (2021).

6. Escobedo, C. On-chip nanohole array based sensing: A review. *Lab Chip* **13**, 2445–2463 (2013).

7. Gomez-Cruz, J. *et al.* Cost-effective flow-through nanohole array-based biosensing platform for the label-free detection of uropathogenic E. coli in real time. *Biosens Bioelectron* **106**, 105–110 (2018).

8. Nair, S., Escobedo, C. & Sabat, R. G. Crossed Surface Relief Gratings as Nanoplasmonic Biosensors. *ACS Sens* **2**, 379–385 (2017).

9. Zhou, J., Khodakov, D. A., Ellis, A. v. & Voelcker, N. H. Surface modification for PDMS-based microfluidic devices. *Electrophoresis* **33**, 89–104 (2012).

10. Prats-Alfonso, E. & Albericio, F. Functionalization of gold surfaces: Recent developments and applications. *J Mater Sci* **46**, 7643–7648 (2011).

11. Victor, A., Ribeiro, J. & F. Araújo, F. Study of PDMS characterization and its applications in biomedicine: A review. *Journal of Mechanical Engineering and Biomechanics* **4**, 1–9 (2019).

12. Torino, S., Conte, L., Iodice, M., Coppola, G. & Prien, R. D. PDMS membranes as sensing element in optical sensors for gas detection in water. *Sens Biosensing Res* **16**, 74–78 (2017).

13. Borok, A., Laboda, K. & Bonyar, A. PDMS bonding technologies for microfluidic applications: A review. Biosensors (2021).

14. MOORE, W. R. *An Introduction to Polymer Chemistry*. *Soil Science* vol. 97 (1964).

15. Lee, J. H. & Han, J. Concentration-enhanced rapid detection of human chorionic gonadotropin as a tumor marker using a nanofluidic preconcentrator. *Microfluid Nanofluidics* **9**, 973–979 (2010).

16. Morbioli, G. G., Speller, N. C. & Stockton, A. M. A practical guide to rapid-prototyping of PDMS-based microfluidic devices: A tutorial. *Analytica Chimica Acta* vol. 1135 150–174 Preprint at https://doi.org/10.1016/j.aca.2020.09.013 (2020).

17. Casanova-Moreno, J. *et al.* Fabricating devices with improved adhesion between PDMS and gold-patterned glass. *Sens Actuators B Chem* **246**, 904–909 (2017).

18. Byun, I., Coleman, A. W. & Kim, B. Transfer of thin Au films to polydimethylsiloxane (PDMS) with reliable bonding using (3-mercaptopropyl)trimethoxysilane (MPTMS) as a molecular adhesive. *Journal of Micromechanics and Microengineering* **23**, (2013).

19. Loo, Y. L., Willett, R. L., Baldwin, K. W. & Rogers, J. A. Additive, nanoscale patterning of metal films with a stamp and a surface chemistry mediated transfer process: Applications in plastic electronics. *Appl Phys Lett* **81**, 562–564 (2002).

20. Ouellet, E., Yang, C. W. T., Lin, T., Yang, L. L. & Lagally, E. T. Novel carboxyl-amine bonding methods for poly(dimethylsiloxane)-based devices. *Langmuir* **26**, 11609–11614 (2010).

21. ISO. Guide ISO/CEI 99 2007 Vocabulaire international de métrologie concepts fondamentaux et généraux et termes associés (VIM). *Vocabulary* **2007**, 1–150 (2006).

22. Bogue, R. Sensors and transducers. *Measurement and Control* **34**, 36 (2001).

23. Fraden, J. *Handbook of Modern Sensors*. *Handbook of Modern Sensors* (Springer International Publishing, 2016).

24. Regtien, P. & Dertien, E. Introduction. in *Sensors for Mechatronics* 1–22 (2018).

25. Webster, J.G., & Eren, H. (Eds.). *Measurement, Instrumentation, and Sensors Handbook*. *Measurement, Instrumentation, and Sensors Handbook* (CRC Press, 2018).

26. Cutkosky, M. R., Howe, R. D. & Provancher, W. R. Force and Tactile Sensors. in *Springer Handbook of Robotics* 455–476 (Springer Berlin Heidelberg, 2008).

27. Jian, M. *et al.* Flexible and Highly Sensitive Pressure Sensors Based on Bionic Hierarchical Structures. *Adv Funct Mater* **27**, (2017).

28. Regtien, P. & Dertien, E. Capacitive sensors. in *Sensors for Mechatronics* 115–144 (Elsevier, 2018).

29. Almassri, A. M. *et al.* Pressure sensor: State of the art, design, and application for robotic hand. *J Sens* **2015**, (2015).

30. Regtien, P. & Dertien, E. Piezoelectric sensors. *Sensors for Mechatronics* 245–265 (2018).

31. Sun, J. J., Hall, A., Simoneishvilli, I., Akdogan, E. K. & Safari, A. *Novel piezoelectric sensors and actuators*. *International Microelectronics and Packaging Society - 3rd IMAPS/ACerS International Conference and Exhibition on Ceramic Interconnect and Ceramic Microsystems Technologies, CICMT 2007* (2007).

32. Regtien, P. & Dertien, E. *Resistive sensors*. *Sensors for Mechatronics* (2018).

33. Fiorillo, A. S., Critello, C. D. & Pullano, A. S. Theory, technology and applications of piezoresistive sensors: A review. *Sens Actuators A Phys* **281**, 156–175 (2018).

34. Park, W.-T. Piezoresistivity. in *Encyclopedia of Nanotechnology* (ed. Bhushan, B.) 3246–3252 (Springer Netherlands, 2016).

35. Chung, D. D. L. A critical review of piezoresistivity and its application in electrical-resistance-based strain sensing. *J Mater Sci* **55**, 15367–15396 (2020).

36. Kalsi, H. S. *Electronic Instrumentation Third Edition*. (2015).

37. de Silva, C. W. *Sensors and Actuators*. (CRC Press, 2015).

38. Tahir, A. M. *et al.* A systematic approach to the design and characterization of a smart insole for detecting vertical ground reaction force (vGRF) in gait analysis. *Sensors (Switzerland)* **20**, (2020).

39. Damilano, A. *et al.* Commercial tactile sensors for hand exoskeletons: Practical considerations for ultra-low cost and very-low complexity read-out. *IEEE Instrum Meas Mag* **19**, 49–56 (2016).

40. Abdul Razak, A. H., Zayegh, A., Begg, R. K. & Wahab, Y. Foot plantar pressure measurement system: A review. *Sensors (Switzerland)* **12**, 9884–9912 (2012).

41. Singh, G., Boddu, S., Chakravorty, I., Bairy, G. M. & Ganesh, M. An instrumented glove for monitoring forces during object manipulation. *IEEE EMBS Special Topic Conference on Point-of-Care (POC) Healthcare Technologies: Synergy Towards Better Global Healthcare, PHT 2013* 212–215 (2013).

42. Schofield, J. S., Evans, K. R., Hebert, J. S., Marasco, P. D. & Carey, J. P. The effect of biomechanical variables on force sensitive resistor error: Implications for calibration and improved accuracy. *J Biomech* **49**, 786–792 (2016).

43. Hall, R. S., Desmoulin, G. T. & Milner, T. E. A technique for conditioning and calibrating force-sensing resistors for repeatable and reliable measurement of compressive force. *J Biomech* **41**, 3492–3495 (2008).

44. Dabling, J. G., Filatov, A. & Wheeler, J. W. Static and cyclic performance evaluation of sensors for human interface pressure measurement. *Proceedings of the Annual International Conference of the IEEE Engineering in Medicine and Biology Society, EMBS* 162–165 (2012).

45. Xiong, L., Chen, P. & Zhou, Q. Adhesion promotion between PDMS and glass by oxygen plasma pre-treatment. *J Adhes Sci Technol* **28**, 1046–1054 (2014).

46. Zhou, H. *et al.* Fast flexible electronics with strained silicon nanomembranes. *Sci Rep* **3**, 1–7 (2013).

47. Sackmann, E. K., Fulton, A. L. & Beebe, D. J. The present and future role of microfluidics in biomedical research. *Nature* vol. 507 181–189 Preprint at https://doi.org/10.1038/nature13118 (2014).

48. Agostini, M., Greco, G. & Cecchini, M. Polydimethylsiloxane (PDMS) irreversible bonding to untreated plastics and metals for microfluidics applications. *APL Mater* **7**, (2019).

49. McClain, M. A. *et al.* Highly-compliant, microcable neuroelectrodes fabricated from thin-film gold and PDMS. *Biomed Microdevices* **13**, 361–373 (2011).

50. Shakeri, A., Khan, S. & Didar, T. F. Conventional and emerging strategies for the fabrication and functionalization of PDMS-based microfluidic devices. *Lab on a Chip* vol. 21 3053–3075 Preprint at https://doi.org/10.1039/d1lc00288k (2021).

51. Rezai, P., Selvaganapathy, P. R. & Wohl, G. R. Plasma enhanced bonding of polydimethylsiloxane with parylene and its optimization. *Journal of Micromechanics and Microengineering* **21**, (2011).

52. Song, K. Y., Zhang, H., Zhang, W. J. & Teixeira, A. Enhancement of the surface free energy of PDMS for reversible and leakage-free bonding of PDMS–PS microfluidic cell-culture systems. *Microfluid Nanofluidics* **22**, (2018).

53. Kim, K., Park, S. W. & Yang, S. S. The optimization of PDMS-PMMA bonding process using silane primer. *Biochip J* **4**, 148–154 (2010).

54. Sang, S. & Witte, H. Fabrication of a surface stress-based PDMS micro-membrane biosensor. *Microsystem Technologies* **16**, 1001–1008 (2010).

55. Lacour, S. P., Wagner, S., Huang, Z. & Suo, Z. Stretchable gold conductors on elastomeric substrates. *Appl Phys Lett* **82**, 2404–2406 (2003).

56. Adrega, T. & Lacour, S. P. Stretchable gold conductors embedded in PDMS and patterned by photolithography: Fabrication and electromechanical characterization. *Journal of Micromechanics and Microengineering* **20**, (2010).

57. Toudeshkchoui, M. G. *et al.* Microfluidic devices with gold thin film channels for chemical and biomedical applications: a review. *Biomed Microdevices* **21**, (2019).

58. Bakouche, M. T. *et al.* Leak-free integrated microfluidic channel fabrication for surface plasmon resonance applications. *Journal of Micromechanics and Microengineering* **30**, (2020).

59. Read, D. T. & Dally, J. W. *A new method for measuring the strength and ductility of thin films*. http://journals.cambridge.org (1993).

60. Jang, S. H., Park, Y. L. & Yin, H. Influence of coalescence on the anisotropic mechanical and electrical properties of nickel powder/polydimethylsiloxane composites. *Materials* **9**, (2016).

61. Kodaira, Y., Miura, T., Takano, Y. & Yonezu, A. Development of biaxial tensile testing for porous polymer membranes. *Polym Test* **106**, (2022).

62. Chen, H. Y., McClelland, A. A., Chen, Z. & Lahann, J. Solventless adhesive bonding using reactive polymer coatings. *Anal Chem* **80**, 4119–4124 (2008).

63. Hoang, M. v., Chung, H. J. & Elias, A. L. Irreversible bonding of polyimide and polydimethylsiloxane (PDMS) based on a thiol-epoxy click reaction. *Journal of Micromechanics and Microengineering* **26**, (2016).

64. Da Silva, L. F. M., Ochsner, A. & Adams, R. D. *Handbook of Adhesion Technology*.

65. Baetens, T., Pallecchi, E., Thomy, V. & Arscott, S. Cracking effects in squashable and stretchable thin metal films on PDMS for flexible microsystems and electronics. *Sci Rep* **8**, (2018).

66. Wang, J., Wang, S., Zhang, P. & Li, Y. Easy-disassembly bonding of PDMS used for leak-tight encapsulation of microfluidic devices. in *2017 18th International Conference on Electronic Packaging Technology (ICEPT)* 1051–1055 (IEEE, 2017).

67. Tang, L. & Lee, N. Y. A facile route for irreversible bonding of plastic-PDMS hybrid microdevices at room temperature. *Lab Chip* **10**, 1274–1280 (2010).

68. Wu, J. & Lee, N. Y. One-step surface modification for irreversible bonding of various plastics with a poly(dimethylsiloxane) elastomer at room temperature. *Lab Chip* **14**, 1564–1571 (2014).

69. Eftekhari, F. *et al.* Nanoholes as nanochannels: Flow-through plasmonic sensing. *Anal Chem* **81**, 4308–4311 (2009).

70. Bdour, Y., Gomez-Cruz, J. & Escobedo, C. Structural stability of optofluidic nanostructures in flow-through operation. *Micromachines (Basel)* **11**, 1–10 (2020).

71. Shardt, Y. A. W. *Statistics for chemical and process engineers: A modern approach*. *Statistics for Chemical and Process Engineers: A Modern Approach* (2015).

72. Electronics, I. *Interlink Electronics Inc., FSR integration Guide and Evaluation parts catalog with suggested Electrical interfaces*. *Version 1.0, 90-45632 Rev. D, 2007.* vol. 1.0, http://www.interlinkelectronics.com/ (2007).

APPENDICES

Appendix A
M5-2, MARK-10

Data Sheet Advanced Digital Force Gauges **Series 5**

32-1111 REV 1020

Series 5 advanced digital force gauges are designed for tension and compression force testing in numerous applications across virtually every industry, with capacities from 0.12 lb to 500 lb (0.5 N to 2500 N). The gauges feature an industry-leading sampling rate of 7,000 Hz, producing accurate results even for quick-action tests. A large, backlit graphics LCD displays large, legible characters, while the simple menu navigation allows for quick access to the gauges' many features and configurable parameters. Data can be transferred to a PC or data collectors via USB, RS-232, Mitutoyo (Digimatic), or analog outputs.

On-board data memory for up to 1,000 readings is included, as are statistical calculations with output to a PC. Integrated set points with indicators and outputs are ideal for pass-fail testing and for triggering external devices such as an alarm, relay, or test stand. The gauges are overload protected to 200% of capacity, and an analog load bar is shown on the display for graphical representation of applied force.

Shown with an ESM303 test stand and G1008 film & paper grips

The Series 5's averaging mode addresses the need to record the average force over time, useful in applications such as peel testing, while external trigger mode makes switch activation testing simple and accurate. An ergonomic, reversible aluminum design allows for hand held use or test stand mounting for more sophisticated testing requirements. Series 5 force gauges are directly compatible with Mark-10 test stands, grips, and software.

MESUR® Lite data acquisition software is included with Series 5 gauges

Series 5 gauges include MESUR® Lite data acquisition software. MESUR® Lite tabulates continuous or single point data from Series 5 gauges. Data saved in the gauge's memory can also be downloaded in bulk. One-click export to Excel easily allows for further data manipulation.

Features

- **High-speed 7,000 Hz sampling rate**
- **USB, RS-232, Mitutoyo, and analog outputs**
- **Large backlit graphic display**
- **1,000-point data memory with statistics and outputs**
- **Live load bar graph with set point markers**
- **Programmable set points, with indicators and outputs**
- **Peak readings and set points always displayed**
- **Averaging mode - calculates average readings over time**
- **External trigger mode - for switch contact testing or remotely stopping display update**
- **Automatic data output via USB/RS-232**
- **5 selectable units of measurement**
- **Configurable audio alarms and key tones**
- **Password protection, configurable for individual keys and calibration**

Focus on Engineering: Reversible Housing

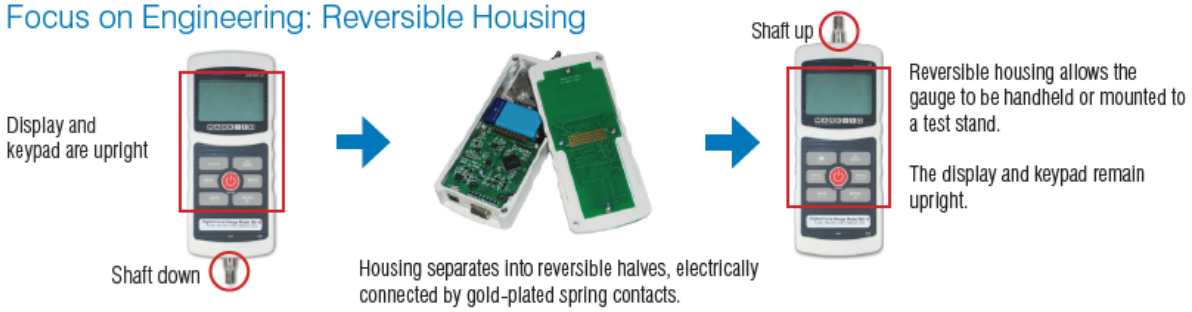

Specifications

Accuracy:	±0.1% of full scale
Sampling Rate:	7,000 Hz
Power:	AC adapter: 100-240VAC, 50-60 Hz, 0.3 A Battery: Rechargeable 8.4V NiMH Low battery indicator appears when battery level is low, and gauge powers off automatically when power reaches critical stage.
Battery life:	Backlight on / off: up to 7 / 24 hours of continuous use
Outputs:	**USB / RS-232:** Configurable up to 115,200 baud. Includes Gauge Control Language 2 for full computer control. **Mitutoyo (Digimatic):** Serial BCD suitable for all Mitutoyo SPC-compatible devices. **Analog:** ±1 VDC, ±0.25% of full scale at capacity, **General purpose:** Three open drain outputs, one input. **Set points:** Three open drain lines.
Configurable settings:	Digital filters, outputs, automatic output (via USB/RS-232), automatic shutoff, default settings, averaging mode, external trigger, passwords, key tones, audio alarms, backlight, calibration
Safe overload:	200% of full scale (display shows "OVER" at 110% and above)
Weight (lb [kg]):	M5-012 - M5-100: 1.0 [0.45], M5-200 - M5-500: 1.2 [0.54]
Load cell deflection:	All models 0.010 [0.25], except 0.005 [0.13] for M5-012
Environmental requirements:	40 - 100°F, max. 96% humidity, non-condensating
Warranty:	3 years (see individual statement for further details)

Appendix B
MECMESIM

Stand-alone Tester

Option 1

MultiTest-*dV* with the Advanced Force Gauge (AFG)

Configuration A: Stand alone tester

The MultiTest-*dV* range integrates perfectly with the Mecmesin AFG, a versatile and fully-featured digital force gauge, available in 10 load capacities from 2.5 N to 2.5 kN with an outstanding accuracy of ±0.1% of full scale.

- Testing to a pre-defined load or crosshead displacement limit
- Testing until a sample break is detected

In its most popular configuration, the combination of MultiTest-*dV* and AFG are ideal for stand-alone applications requiring the capture on a display of a peak load value.

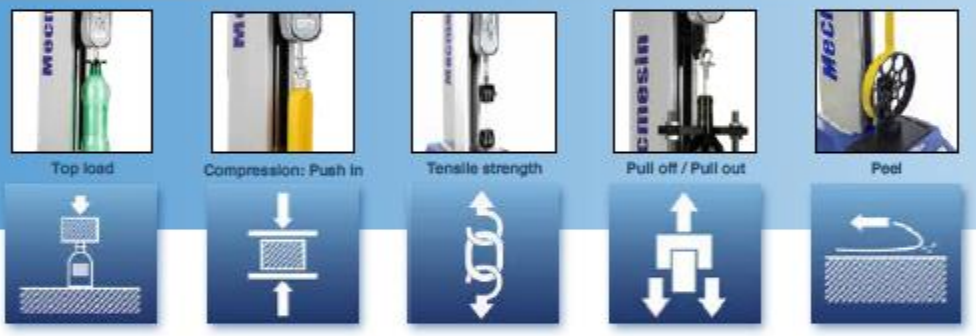

Configuration B: Expand product testing capabilities with VectorPro Lite software

With the appropriate communications cables, data can be streamed from the AFG via the MultiTest-*dV* to VectorPro Lite data-acquisition software to collect the values of load, displacement and time.

It is ideal for applications where the true physical characteristics of the specimen cannot be detected by peak-load only and require a graphical presentation to highlight specific events during the test.

See pages 6-8 for more details of VectorPro Lite software

Specifications

MultiTest-*dV*		0.5	1	2.5
Rated capacities	kN	0.5	1.0	2.5
	kgf	50	100	250
	lbf	110	220	550
Displacement				
Crosshead travel*		1186 mm (46.7")	986 mm (38.8")	507 mm (20")
Maximum headroom*		1205mm (47.4")	1005mm (39.6")	526mm (20.7")
Displacement resolution	mm	0.001	0.001	0.001
	in	0.000025	0.000025	0.000025
Positional accuracy		±0.130/300 mm (±0.005/11.81")	±0.130/300 mm (±0.005/11.81")	±0.130/300 mm (±0.005/11.81")
Speed				
Speed range†	mm/min	0.1 to 1200	0.1 to 1200	0.1 to 1200 ††
	in/min	0.004 to 47.2	0.004 to 47.2	0.004 to 47.2
Speed accuracy		±2% of indicated speed or ±20 µ/min, whichever is greater		
Speed resolution	mm/min	0.1	0.1	0.1
	in/min	0.004	0.004	0.004
Maximum no. of cycles per test		9999		
Dimensions				
Height		1616 mm (64")	1416 mm (56")	941 mm (37")
Width		290 mm (11.4")	290 mm (11.4")	290 mm (11.4")
Depth		414 mm (16.3")	414 mm (16.3")	414 mm (16.3")
Vertical daylight		1267mm (49.9")	1067mm (42")	588mm (23.1")
Throat depth**		70.5 mm (2.8")	70.5 mm (2.8")	70.5 mm (2.8")
Weight		26 kg (57 lb)	25 kg (55 lb)	24 kg (53 lb)
Electrical supply				
Voltage		230 V AC 50 Hz / 110 V AC 60 Hz	230 V AC 50 Hz / 110 V AC 60 Hz	230 V AC 50 Hz / 110 V AC 60 Hz
Maximum power requirements		120 W	200 W	250 W
Advanced Force Gauge (AFG), 10 models from 2.5 N to 2500 N				
Accuracy***		±0.1% of full-scale		
Enhanced Load Sensors (ELS), 13 models from 2.5 N to 2500 N				
Accuracy		±0.5% of reading down to 5% of range		

* Measured with force gauge and short extension rod fitted. ** Measured on centreline of gauge/sensor.

*** Due to the variety of environmental conditions the device may be used in, this value does not include uncertainty of measurement.

† Where mains voltage is reliable. †† 2.5 kN: recommended maximum speed = 750 mm/min (30 in/min) above 2 kN.

Common Specifications	
Operating temperature	10°C – 35°C (50°F – 95°F)
Digital display of Load/Position/Speed	Yes
Output of test results to PC/Printer	Yes, via USB

Interface Cables

Part no.	Description
351-092	Interface cable, AFG (15-pin RS232), to MultiTest-*dV* stands (RJ11) – 2 m long
352-275-V01	Interface cable, ELS (HR10), to MultiTest 0.5-*dV* and MultiTest 1-*dV* stand (HR10) – 1.2 m long
352-275	Interface cable, ELS (HR10), to MultiTest 2.5-*dV* stands (HR10) – 0.6 m long
351-093	Interface cable, MultiTest-*dV* test stands (USB B) to PC (USB A) – 2 m long

Software and communications	
PC requirements (recommended)	Intel Core i5 processor, 8 GB RAM, one USB 2.0 or 3.0 port, SSD hard drive with 10 GB free space, screen resolution 1920x1080 full HD
PC requirements (minimum)	Intel/AMD dual core processor with 2 GHz or faster clock speed, 4 GB RAM, one USB 2.0 or 3.0 port, hard drive with 10 GB free space, screen resolution 1080x720

Appendix C
Sensor FSR07 datasheet.

INTERLINK ELECTRONICS

FSR® 400 Series Data Sheet

Force Sensing Resistors®

Features and Benefits

- Actuation force as low as 0.2N and sensitivity range to 20N
- Cost effective
- Ultra thin
- Robust; up to 10M actuations
- Simple and easy to integrate

Description

Interlink Electronics FSR® 400 Series is part of the single zone Force Sensing Resistor® family. Force Sensing Resistors, or FSR's, are robust polymer thick film (PTF) devices that exhibit a decrease in resistance with increase in force applied to the surface of the sensor. This force sensitivity is optimized for use in human machine interface devices including automotive electronics, medical systems, industrial controls and robotics.

The FSR 400 Series sensors come in seven different models with four different connecting options. A battery operated demo is available. Call us for more information at +1 805-484-8855.

FSR® 400 Short
5mm Circle x 20mm

FSR® 400
5mm Circle x 38mm

FSR® 402 Short
13mm Circle x 25mm

FSR® 402
13mm Circle x 56mm

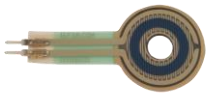

FSR® 404
20mm Donut with 5.5mm hold

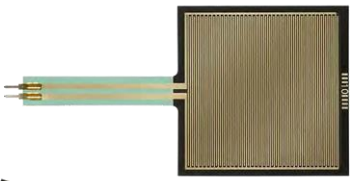

FSR® 406
38mm Square x 83mm

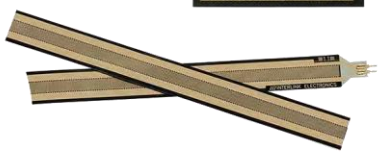

FSR® 408-xxx
10mm Wide x xxx mm strip
xxx = 50, 100, 200, 300, 400, 500mm

P/N: PDS-10004-C

Human-Machine Interface Solutions for a Connected World

INTERLINK ELECTRONICS

FSR® 400 Series Data Sheet

Force Sensing Resistors®

Device Characteristics

Actuation Force*	~0.2N min
Force Sensitivity Range*	~0.2N – 20N
Force Resolution	Continuous (analog)
Force Repeatability Single Part	+/- 2%
Force Repeatability Part to Part	+/- 6% (Single Batch)
Non-Actuated Resistance	>10 Mohms
Hysteresis	+10% Average (RF+ - RF-)/RF+
Device Rise Time	< 3 Microseconds
Long Term Drift	
1kg load, 35 days	< 5% log10(time)
Operating Temperature Performance	
Cold: -40ºC after 1 hour	-5% average resistance change
Hot: +85ºC after 1 hour	-15% average resistance change
Hot Humid: +85ºC 95RH after 1 hour	+10% average resistance change
Storage Temperature Performance	
Cold: -25ºC after 120 hours	-10% average resistance change
Hot: +85ºC after 120 hours	-%5 average resistance change
Hot Humid: +85ºC 95RH after 240 hours	+30% average resistance change
Tap Durability	
Tested to 10 Million actuations, 1kg, 4Hz	-10% average resistance change
Standing Load Durability	
2.5kg for 24 hours	-5% average resistance change
EMI	Generates no EMI
ESD	Not ESD Sensitive
UL	All materials UL grade 94 V-1 or better
RoHS	Compliant

Specifications are derived from measurements taken at 1000 grams, and are given as (one standard deviation/mean), unless otherwise noted.
*Typical value. Force dependent on actuation interface, mechanics, and measurement electronics.

INTERLINK ELECTRONICS

FSR® Model 402

Force Sensing Resistor®

Model 402:

Active Area: Ø14.68mm
Nominal Thickness: 0.46mm
Switch Travel: 0.15mm

Available Part Numbers:

PN: 44-29103 Model 402
- No contacts or solder tabs

PN: 34-00012 Model 402
- with female contacts

PN: 34-00001 Model 402
- with female contacts and housing

PN: 30-81794 Model 402
- with solder tabs

Sensor Mechanical Data

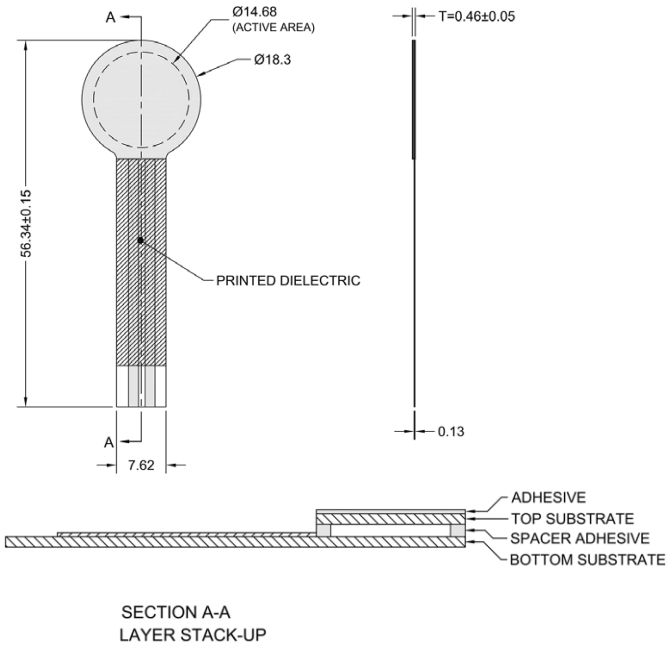

SECTION A-A
LAYER STACK-UP

Exploded View

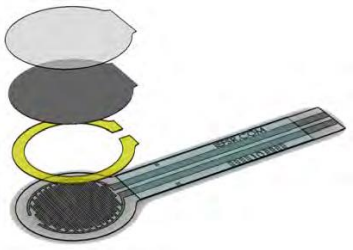

Appendix D

FSR sensor electrical circuit.

The system uses an operational amplifier (Op-Amp) LM358N. This device is suitable for the system because of its electric characteristics, such as, the slew rate and the bandwidth values. Also, this Op-Amp was selected because it can be used for both proposed circuits, Wheatstone Bridge circuit and Inverter Voltage circuit, thus we compared them. On Figure 37 the electric circuit is displayed and based on the sensor's manufacturer guide; the next expression was obtained:

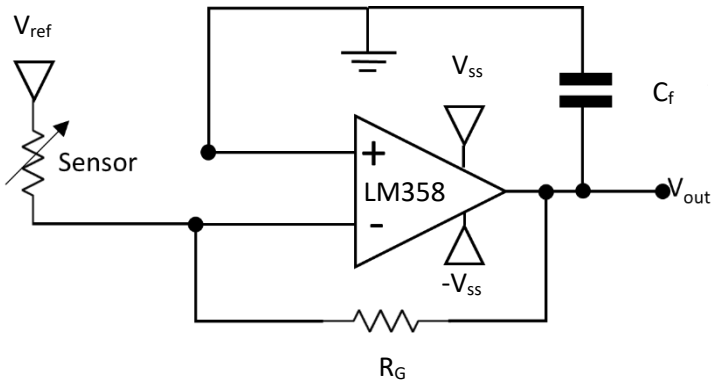

Figure 37 Voltage inversor using the Op-Amp LM358.

$$V_{out} = V_{ref}.\left(-\frac{R_G}{R_{sensor}}\right)$$

This is an inverter circuit, then the reference voltage used to source the sensor, should be negative, to obtain a positive value in the output. It is important to know that the gain resistor R_G is a constant value of $2.23\ k\Omega$, and the sensor resistance will vary between $10\ M\Omega$ and $1\ k\Omega$ when a force of 1 kg is applied. By considering these values, and the reference voltage as $-5V$ the expression should be:

$$V_{out} = \left(\frac{11.35}{R_{sensor}}\right)[V]$$

Appendix E

Stepper motor electrical circuit

The stepper motor oversaw moving the samples through the test, to perform this task, the motor used is attached to this system by using a base shown in Figure 14. On this project we use a bipolar stepper motor and to control it uses a driver A4988, this driver allows to control the number of steps and the direction. Also, this driver can perform micro steps by dividing the steps of the motor. However, the aim of this work is to use a micrometer, which has a suitable resolution per step, attached to this stepper motor, thus we don't need to use the micro steps. In Figure 38 the motor circuit is shown, this circuit uses a driver A4988, a bipolar stepper motor and a microcontroller Arduino Uno. Figure represents the electrical circuit used for this work.

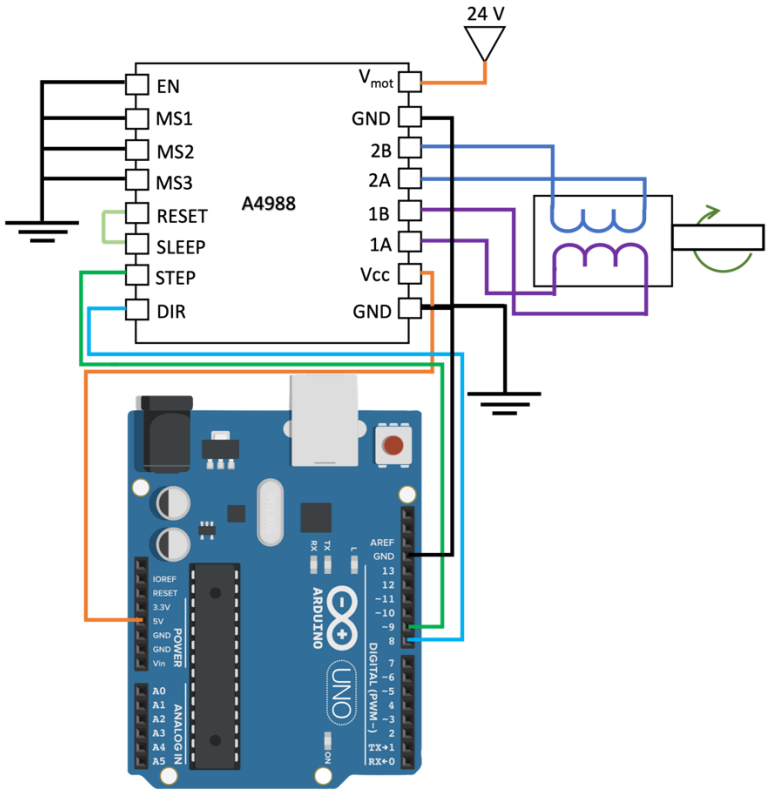

Figure 38 Motor electrical circuit